PEOPLE'S DEMOCRATIC REPUBLIC OF ALGERIA

MINISTRY OF HIGHER EDUCATION AND SCIENTIFIC RESEARCH

MOHAMED BOUDIAF UNIVERSITY– M'SILA

FACULTY: TECHNOLOGY

DEPARTMENT: ELECTRONICS

No:

DOMAIN: SCIENCES AND TECHNOLOGY

SECTOR: ELECTRONICS

OPTION: MICROELECTRONICS

Thesis submitted for obtaining

Academic Master's degree

By: DELLOUM Amira

ZOUBIRI Zakaria

Entitled

MODELING OF A TEMPERATURE SENSOR BASED ON PLASMONIC STRUCTURES

Defended before the jury composed of:

Dr.BOURAS Mounir	University of M'sila	Jury president
Pr.HOCINI Abdsselem	University of M'sila	Supervisor/Reporter
Dr.ZOUACHE Tarek	University of M'sila	Co-supervisor
Dr.KAHLOUCHE Ahmed	University of M'sila	Examiner

Academic year: 2019/2020

Acknowledgements:

First of all, we thank Almighty GOD, who has given us the courage, strength and will to carry out this modest work.

First of all, I would like to express my gratitude and recognition to Mr. Pr.A. Houcini, Professor at the University of M'sila, for supervising and supporting me during the completion of this work. I also thank him for his invaluable help, the advice and the knowledge which he was able to make me benefit. It is difficult for us to express in a few words how much admiration I have for him.

Also our warm thanks extend to the co-supervisor Dr.Zouach Tarek for his help and support throughout this work and his significant aid till the end of this work.

Our warmest thanks to Marouan Bouchouachi for his help, guidance and availability, also for the trust, patience and understanding he has always shown us.

My thanks go to all the members of the jury, for agreeing to sit in my defense as examiners.

We would like to thank our parents because this work represents a small fruit of their suffering and which without them we cannot get through these long years of study and work.

Finally, we thank all who contributed from near or far for their moral or material support and the development of this work.

Dedications

I dedicate this work:

To my dear parents who supported me throughout my studies, I wish them good health, may ALLAH protect them. Souls very dear sisters and my very dear brothers.

To the whole family and All my friends.

To the former dean of the college Previous and current.

To all those who love me and whom I love and to the late Khaled Zedlkhir.

To all the teachers who have contributed to my training throughout my studies to date.

AMIRA DELLOUM

Dedication:

I dedicate this humble work to my family, friends and whoever helped me take a step forward throughout my life in general and this work in particular.

ZOUBIRI Zakaria

Abstract:

Sensor technologies have evolved significantly throughout the years and specifically the ones based on plasmonics and surface plasmons phenomenon which are excitations of the collective electrons on the surface of metals and since their discovery researchers sought to implement this phenomenon for the unique properties offered by this technology, this works goes through the basic explanation of this phenomenon then its application in sensors and finally a study of a proposed plasmonic sensor for the specific function as temperature sensor.

ملخص:

تكنولوجيا الحساسات تطورت عبر السنوات بشكل كبير وخاصة التي تعتمد على البلازمونيك وظاهرة بلازمونات السطح والتي هي عبارة عن تحفيز لمجموع الكترونات أسطح معادن ومنذ اكتشافها سعا الباحثون لإدماج هذه الظاهرة بسبب الخصائص الفريدة التي توفرها هذه التكنولوجيا, هذا العمل يمر خلال الشرح الأساسي للظاهرة وتطبيقها على الحساسات وفي الأخير دراسة على حساس بلازمونيك مقترح للوظيفة المتخصصة كحساس درجة حرارة.

List of tables:

List of figures:

Contents:

General introduction

Data communication and information processing are driving the rapid development of ultra-high speed and ultra-compactness in nano-photo-electronic integration. Plasmonic technology has in recent years demonstrated the promise to overcome the size mismatch between microscale photonic and nanoscale electronic integration, and it likely will be crucial for the next generation of on-chip optical nano-interconnects, enabling the deployment of small-footprint and low-energy integrated circuitry.

The phenomenon of surface plasmons was first observed in the Lycurgus cup, which is a Roman glass cage cup in the British Museum, London, UK, also the first documented observation of surface plasmon waves dates back to 1902 and results from the work of R.W. Wood[1]. The latter illuminated a metallic diffraction grating with white (or polychromatic) light and found anomalies in the diffraction spectrum, taking the form of narrow dark bands. A few decades later, the theoretical work of U. Fano in 1941 made it possible to conclude that these anomalies were associated with the excitation of electromagnetic surface waves on the edge of the diffraction grating [2]. In 1952, D. Bohm and D. Pines introduced electron plasma in a metallic solid to explain the energy losses due to fast electrons passing through a metallic sheet. They called this excitement a plasmon[3]. In 1965, A. Hessel and A. Olier proposed a more general theory of Wood anomalies for metal networks. They interpret these anomalies by the effects of resonance from the coupling between the incident wave and the natural modes of the network. It was in 1968 that A. Otto showed that these surface waves can be excited using attenuated total reflection. In the same year, Kretschmann and Reuther obtain the same results from a different configuration of the attenuated total reflection method, following these the interest in surface plasmons has increased considerably, particularly in characterizing thin films and in studying processes taking place on metal interfaces. Also, the great propagation length of these surface waves (several lengths of waves) induces a coherence of the field confines on the interface [5]. And on the other hand, the high energy density it carries (these surface waves) is also a very interesting of the existence of these surface waves on certain materials [13] this type of excitation is rather qualified as a volume plasmon, to be distinguished from surface plasmons. Although surface electromagnetic waves were first discussed by A. Sommerfeld and J. Zenneck, R. Ritchie. In the last few decades, the phenomenon of surface plasmons has been extensively studied both theoretically and experimentally, and there have been attempts to use it for various applications ranging from solar-cell energy and sensing to nanophotonic devices.

The thesis consists of 3 chapters; Chapter 1 provides an introduction to the plasmonics and properties of surface plasmons. Within this Chapter we shall present a brief explanation of interactions between light and metal and the theory of electromagnetic surface plasmons written on the basis of theoretical analysis of light propagation in planar metal/dielectric waveguides, along with the principal characteristics of SP's propagating along metal-dielectric and metal-dielectric-metal waveguides are introduced and discuss shortly the SP's optical excitation methods.

Chapter 2 introduces the fundamentals of plasmonic sensors characteristics and their modeling methods along with an example of a MIM based temperature sensor.

Chapter 3 presents the modeling and simulation steps of our proposed plasmonic sensor structure using the software Rsoft, which implements a time-domain simulation method, in particular the finite-difference time-domain method (FDTD).

Chapter I: Surface Plasmons

I.1 Introduction:

In 1956 an article by D.Pines where he put a name on the confined wave, the choice of name by the fact that "the collective oscillations of valence electrons resemble strongly to the oscillations of the plasma in the gas discharges ". The oscillation of the "plasma electronics" then became plasmon [3]. and after that in 1958 Turbadar detected a big decrease in the reflectivity when illuminating thin metalic layers on a substrate [4].in 1968 Otto managed to explain Turbadar's conclusions and describe that the drop in reflectivity and attenuated total reflection method is caused by the excitation of Surface Plasmons [5]. Within the same year Kretshmann and Raether reported excitation of surface plasmons with another configuration of the attenuated total reflection method [6]. The unprecedented work of Otto, Krestschmann and Raether founded a convinient excitation method for surface plasmons and their research brought surface plasmons to the modern field of optics. In the late 70's surface plasmons were implemented in the characterization of thin films [7] and the studying of processes at metal boundaries [8]. The high sensitivity of the plasmon to the index variation of a medium then becomes a tool for measuring variations in an environment, and for example a solution and The short propagation length of the plasmon makes it possible to design circuits with even smaller dimensions, which is of great interest to telecommunications [9].

Within this chapter we shall present an explanation of interactions between light and metal and the theory of elctromagnetic surface plasmons written on the basis of theoretical analysis of light propagation in planar metal/deilectric waveguides, along with the principal characteristics of SP's propagating along metal-deilectric and metal-deilectirc-metal waveguides are introduced and discuss SP's optical excitation methods, and the associated modes finishing with examples of applications.

I.2. Surface plasmon and surface plasmon mode :

I.2.1 optical response of metals:

Bulk material optical properties, such as its color, can be described with the material's relative permittivity or dielectric function ε. In the simplest approximation, metals are described as a free electron gas with the metals dielectric function ε_m noted:

$$\varepsilon_m(\omega) = 1 - \frac{\omega_p^2}{\omega^2} \qquad \textbf{Eq.I.1}$$

Where ω is the angular frequency of light and ω_p the plasma frequency of the metal ($\omega_p \approx 1.4 \times 10^{16}\ Hz$ for gold) [10]. The dielectric function of the metal is dependent on the frequency that $\varepsilon_m < 0$ for frequencies blow plasma frequency and $\varepsilon_m > 0$ for frequencies above the plasma frequency. This results for a refractive index which is the square root of the dielectric function ($n = \sqrt{\varepsilon}$) to be imaginary and real for frequencies below and above ω_p ,respectively. For metals like gold and silver, the frequency of visible light is below ω_p, resulting in an imaginary refractive index and high reflectivity (mirror like) surfaces.

The damping of electrons motion due to inelastic processes such as collisions in the material can be accounted for by adding the damping frequency γ according to:

$$\varepsilon_m(\omega) = 1 - \frac{\omega_p^2}{\omega^2 + i\gamma\omega} \qquad \textbf{Eq.I.2}$$

The dielectric function according to Drude's model is a two component formula ($\varepsilon_m = \varepsilon_m{}' + i\varepsilon_m{}''$) with the components being:

$$\varepsilon_m{}'(\omega) = 1 - \frac{\omega_p^2}{\omega^2 + \gamma^2} \qquad \textbf{Eq.I.3}$$

$$\varepsilon_m{}''(\omega) = \frac{\omega_p^2\gamma}{\omega^3 - \omega\gamma^2} \qquad \textbf{Eq.I.4}$$

For UV-visible-NIR frequencies, ω is in the order of $1 - 10 \times 10^{15}$Hz. So for typical noble metals such as gold ($\gamma_{gold} \approx 4 \times 10^{13} Hz$) [10] γ is less than ω. This implies that $\varepsilon_m{}''$ is low in frequency range and the $\varepsilon_m{}'$is almost the same as that described without the damping factor Eq.I.1.

Depending on the above, metals dielectric function approaches 1 at high frequencies ($\omega >> \omega_p$). Typically this is not case for a real metal such as gold due to, for example, the influence of positive background of the metal ion cores. This can be taken in consideration by replacing the first terms in Eq.I.2 with ε_∞ (typically between 1 and 10)[10], which is the value that ε_m approaches when $\omega \to \infty$ [12]:

$$\varepsilon_m(\omega) = \varepsilon_\infty - \frac{\omega_p^2}{\omega^2 + i\gamma\omega} \qquad \textbf{Eq.I.5}$$

I.2.2 Surface plasmon:

The surface plasmon is conventionally defined as the variation of the collective oscillation of electrons at the interface of a metal and a dielectric. To excite a surface plasmon, it is necessary to guarantee the frequency agreement between the oscillation of the electrons and the incident exciting wave. The electrons then oscillate at the resonant frequency ω_p (or plasma frequency) if we consider the free electrons as a gas.

To understand the phenomenon in more detail, we propose an approach by solving the Maxwell equations at the interface of a dielectric and a metal. The dispersion relation at the interface of a semi-infinite metal (see Figure 1) of permittivity $\varepsilon_m = \varepsilon_m^{'} + i\varepsilon_m^{''}$ and of a dielectric of permittivity $\varepsilon_d$is written:

$$\frac{k_{zm}}{\varepsilon_m} + \frac{k_{zd}}{\varepsilon_d} \qquad \textbf{Eq.I.6}$$

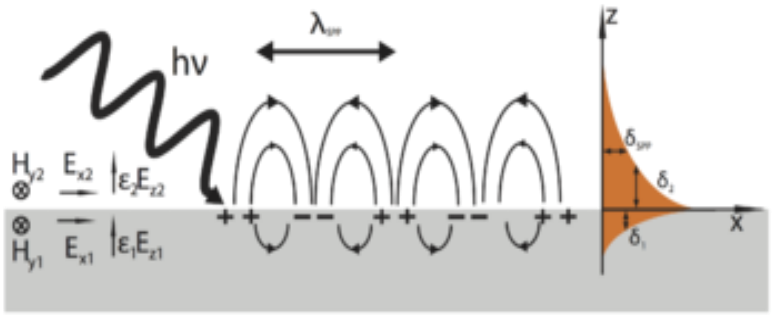

Figure 1 Schematic representation of a SP at a metal-dielectric interface.the exponential decrease of the electromagnatic field is represented on the right .

With k_{zm} and k_{zd} the wave vectors parallel to the z direction in the respective media m (metal) and d (dielectric). If we decompose the free space wave vector, defined by $k_0 = \frac{2n}{\lambda}$ with λ the wavelength, we get :

$$\varepsilon_i k_0^2 = k_x^2 + k_{zi}^2 \qquad \textbf{Eq.I.7}$$

From where $k_{zi} = [\varepsilon_i k_0^2 - k_x^2]^{1/2}$ with i=1,2.

So by expressing kx with equations (1) and (2) we obtain:

$$k_x = k_0 \left(\frac{\varepsilon_m \varepsilon_d}{\varepsilon_m + \varepsilon_d} \right)^{1/2} \quad \textbf{Eq.I. 8}$$

The vector kx which represents the wave vector in the x direction is the expression of the wave vector of the plasmon. So we can describe kx by a complex wave vector.

such that $k_x = k_x^{'} + ik_x^{''}$it comes then:

$$k_x^{'} = k_0 \left(\frac{\varepsilon_m^{'} \varepsilon_d}{\varepsilon_m^{'} + \varepsilon_d} \right)^{1/2} \quad \textbf{Eq.I. 9}$$

$$k_x^{''} = k_0 \times \left(\frac{\varepsilon_m^{'} \varepsilon_d}{\varepsilon_m^{'} + \varepsilon_d} \right)^{3/2} \times \left(\frac{\varepsilon_m^{''}}{(2\varepsilon_m^{'})^2} \right) \quad \textbf{Eq.I. 10}$$

For $k_x^{'}$ to be real, the following conditions must be satisfied : $\varepsilon_m^{'} < 0$et $\left|\varepsilon_m^{'}\right| > \varepsilon_d$. These two conditions can be satisfied mainly in metal. kx ′ then expresses the free space wave vector multiplied by the effective plasmon index for this given wavelength. So we can write:

$$k_x^{'} = k_0 \left(\frac{\varepsilon_m^{'} \varepsilon_d}{\varepsilon_m^{'} + \varepsilon_d} \right)^{1/2} = n_e k_0 \quad \textbf{Eq.I. 11}$$

with $n_e = \left(\frac{\varepsilon_d \varepsilon_m^{'}}{\varepsilon_m^{'} + \varepsilon_d} \right)^{1/2}$

This approach is identical to optical modes such as those described in waveguides, which will make it possible to understand the excitation conditions of the modes in a similar way. As for the vector $k_x^{''}$, it expresses the internal absorption of the plasmon as it propagates along the x axis. Maintenant que nous avons décrit les conditions d'existence du plasmon de surface ainsi que son vecteur d'onde, intéressons-nous à sa propagation le long de l'axe x. It is known that these surface plasmons can be devided into two sub groups, according to thier propagation distance :localised surface plasmons and delocalised surface plasmons or extended.

I.2.3 localised surface plasmons :

surface plasmon exist in metalic nanoparticles different from delocalised SP's with different properties: the effect of size and nature of metalic particles have a significant influence on the condition of resonance. These surface plasmons are radiative and can be coupled directly to light. They present a stong confinement of electomagnatic field near the metalic particles and they don't propagate except a nanometric distances. This confinement play and essential role in surface Raman scattering (SERS effect)that is based on enhancing of the electromagnetic field near the particles.

I.2.4 Surface Plasmon Polaritons:

First predicted by Ritchie in 1957[13], SPP are an electromagnetic excitation of collective oscillations of the conduction electrons near a metal surface. The SPP propagates as a wave at the interface between a metal and a dielectric medium. And because the SPPs are transverse magnetic waves the magnetic field oscillates in the plane of the interface. The accompanying electric fields of the SPP have a longitudinal component in the direction of the propagation and components perpendicular to the interface that decay exponentially into both the metal and the dielectric medium (see Figure 2(a))[11]. The carry momentum of the SPPs, described by wave vector k_{SPP} .The magnitude of wave vector is given by the dispersion relation:

$$k_{SPP} = \frac{\omega}{c}\sqrt{\frac{\varepsilon_m(\omega).n^2}{\varepsilon_m(\omega)+n^2}} \qquad \textbf{Eq.I.12}$$

Where n is the refractive index of the dielectric medium and *c* the speed of light in vacuum. From the derivation of Eq.I.12[16], It is clear that SPPs are supported only if the real components of the dielectric functions of the two interface materials are opposite in sign. Hence, the condition between metal (below its plasma frequency so that $\varepsilon_m{}' < 0$) and the dielectric medium with a dielectric function $\varepsilon = n^2$ is both real and positive must be fulfilled at the interface. It's noted that with a complex metal dielectric function, Eq.I.12 gives a complex wave vector. Where the imaginary part corresponds to losses in the system and states how far the SPP will propagate on the surface. When the imaginary component of the dielectric function is small($\varepsilon_m{}'' << |\varepsilon_m{}'|, as\ for\ gold\ in\ the\ visible\ region$), the real part of the wave vector can be approximated from Eq.I.12 by neglecting the imaginary component of ε_m.

Because $\varepsilon_m{}' < 0$ (and$|\varepsilon_m|' > n^2$) for the allowed frequencies, we have from Eq.I.12:

$$k_{SPP} > \frac{\omega}{c} n \qquad \textbf{Eq.I.13}$$

The right side of Eq.I.13 is equal to the wave number for light at frequency ω traveling in the same dielectric medium. And the momentum of the SPP is parallel to the surface; the momentum component of the photon parallel to the surface is the relevant to the excitation of SPPs. For light travelling in the dielectric towards the metal surface at an angle θ, the wave number component parallel to the surface is:

$$k_{photon} = \frac{\omega}{c} n \cdot sin\theta < \frac{\omega}{c} n \qquad \textbf{Eq.I.14}$$

From Eq.I.13 and Eq.I.14 the following relation is obtained for any given frequency regardless of the incidence angle:

$$k_{photon} < k_{SPP} \qquad \textbf{Eq.I.15}$$

This means that the SPPs will not radiate into the dielectric medium and also that light (incident on the surface in this way) cannot excite SPPs. The reason is both the frequency (energy) and the wave vector (momentum) must be conserved in the conversion of photons to SPPs or vice versa. Figure 2(b) illustrates graphically the dispersion relations for light in air and SPPS at a metal/air interface do not coincide. The straight line shows the dispersion relation for light parallel to the metal surface and the shaded area represents all possible incidence angles (the light cone). It I obvious the photons have too small wave vectors in order to excite SPPs. while the dispersion relation for light is linear, the dispersion curve for the SPP is not, and approaches $\omega_p(1 + n^2)^{-1/2}$ for large values of k_{SPP}.

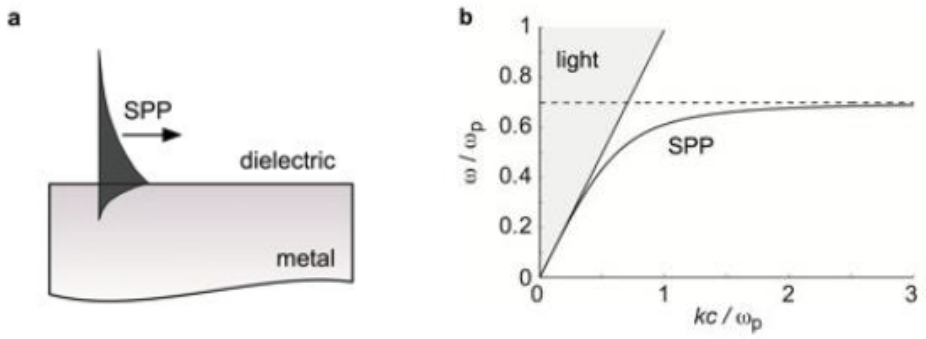

Figure 2 : (a) Schematic illustration of a SPP propagating at the interface between a metal and a dielectric material. The regions illustrate the exponentially decaying fields in both materials. (b) Dispersion relations for the SPPs at a gold/air interface and light in air (*n*=1). For the latter, the wave vector parallel to the surface is used and filled area represents all possible angles of incidence (the light cone). The dashed line indicates that the frequency of the SPP approaches $\boldsymbol{\omega_p(1+n^2)^{-1/2}}$ for large wave vectors.

I.3 Coupling and optical excitation of SPPs:

In 1968, Kretschmann and Raether [6] and Otto [5] presented methods that enable the excitation of SPPs on a flat metal film using light. The Kretschmann configuration is illustrated schematically in Figure 3(a), for a sufficiently thin metal film, the evanescent field from light totally reflected at the glass/metal interface can excite SPPs at the metal/air interface (*n*=1) when the following condition is met:

$$k_{photon} = k_{SPP} \Rightarrow \qquad \textbf{Eq.I.16}$$

$$n_{prism} \cdot \sin(\theta) = \sqrt{\frac{\varepsilon_m(\omega).n^2}{\varepsilon_m(\omega)+n^2}} \qquad \textbf{Eq.I.17}$$

Either the frequency (wavelength) or the angle of incidence (or both) can be tuned to find solutions to Eq.I.17. Also the process works the other way around; SPPs excited in this way are inherently leaky and can couple out as electromagnetic radiation into the prism [11]. In both the angular and frequency spectra, a dip corresponding to SPP excitation appears due to absorption in the metal combined with destructive interference between directly reflected light and light that is reemitted from SPPs [11].

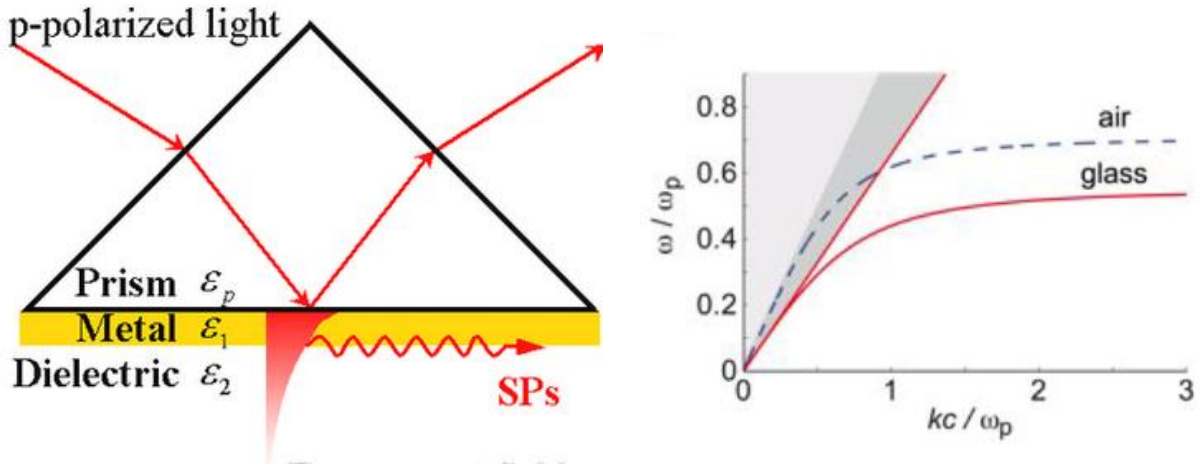

Figure 3 : (a) Schematic of the Kretschmann configuration illustrating how SPPs at the metal/air interface can be excited using light incident through a glass prism from the back of the thin metal film. (b) Dispersion relations for SPPs at a gold/air (dashed trace) and a gold/glass (solid trace) interface. Also shown is the dispersion of light in glass (straight curve) where the shaded grey areas represent all angles of incidence and the darker shaded area represents angles of incidence that can excite SPPs at the metal/air interface.

I.3.1 coupling of a surface plasmon:

In order to satisfy the synchronism between an incident wave and a plasmon mode. as is the case with optical waveguide modes, the two wave vectors must be equal, which we can translate as :

$$k_{x'} = k_p = k_0 n_d sin(\theta) \qquad \textbf{Eq.I. 18}$$

With k_p wave vector of the confined plasmon along the x axis and $k_0 n_d sin(\theta)$ wave vector of the incident wave in a dielectric medium of index n_d with an angle of incidence (θ). We noted previously that $k_x^{'} = n_e k_0$ or n_e , the effective plasmon index, is always greater than n_d. Equality (Eq.I. 10) is not satisfied as it is, and it is not possible to couple a plasmon without the contribution of an additional constant or variable. To be able to couple an incident wave to a plasmon, the following conditions must then be met:

$$k_p = k_0 n_d sin(\theta) A \qquad \textbf{Eq.I. 19}$$

With A the parameter making it possible to satisfy equality (Eq.I. 19). We will thus present two ways to satisfy this equality and allow the excitation of a plasmon mode.

I.3.1.1 Coupling of a surface plasmon by a prism:

This method consists in creating a total internal reflection at a dielectric-metal interface, in order to create an evanescent wave on said interface. If the thickness of the metal layer is thin enough the evanescent wave penetrates the metal layer and can couple the surface plasmon of the other metal-dielectric interface (see Figure 4) [6].

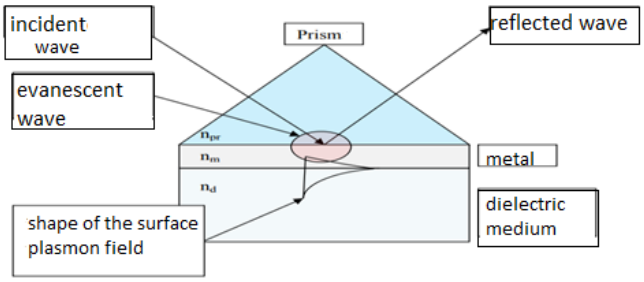

Figure 4 : Excitation of a surface plasmon in the Kretschmann-Raether configuration.

The particularity of this method lies in the dielectric dissymmetry npr and nd. Indeed to guarantee the coupling of the surface plasmon with the evanescent wave propagating in the prism, it is necessary that $n_{pr}>n_d$. Under this condition it is then possible that nd≥np, with np the effective index of the surface plasmon propagating at the metal-dielectric interface of index nd. we can then write the following equality:

$$k_0 n_p sin(\theta) = k_p \qquad \textbf{Eq.I. 20}$$

Now suppose, as in Figure 4, a prism with a face covered with a metal. The thickness is finite of value q, and we consider the thickness of the prism. Equation (Eq.I. 18) then becomes :

$$k_0 n_p sin(\theta) = k_{sp0} + \Delta A = k_{sp} \qquad \textbf{Eq.I. 21}$$

With ΔA taking into account the presence of the prism and the finite thickness of the metal and k_{sp} the surface plasmon vector integrating the entire device of Figure 4.

Assuming that | ε'm | >> nd and that | ε'm | >> ε'm then we can express the coefficient ΔA such that :

$$\Delta A = r_{pm} e^{2ik_{xmq}} k_0 \sqrt[3]{\left(\frac{\varepsilon_d \varepsilon_m}{\varepsilon_d \varepsilon_m} \frac{1}{\varepsilon_d - \varepsilon_m}\right)} \qquad \textbf{Eq.I. 22}$$

With r_{pm} the reflection coefficient at the prism-metal interface, the k_{xm} wave vector propagating along the x axis, and q the thickness of the metal layer. The maximum surface plasmon excitation is obtained when the reflectivity R(θ,λ)=0, that is, when the energy of the incident wave is completely dissipated in the surface plasmon. For this, the radiative losses Уrad must be equal to the absorption losses Уa, Уrad = Уa.

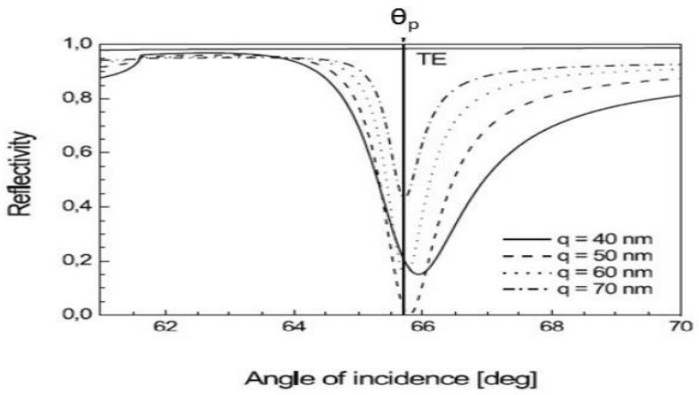

Figure 5 : Variation in reflection as a function of the thickness of the metal. Device Kretschmann-Raether with a BK7 prism, gold metal layer and water for the last dielectric interface. Incident wave λ = 800 nm polarization TM, TE only presented here for comparison. [14]

As we can observe in Figure 5, the minimum of reflection is reached for a single thickness of metal, here of 50 nm. The angle θ_p indicates the angular position of the surface plasmon resonance, for the Kretschmann-Raether configuration and for a fixed wavelength of 800 nm.

There is another configuration, much less used, which we will quote here as an example in order to be complete in the presentation of the coupling devices. This second device using a prism is called an “Otto” device [5]. (see Figure 6).

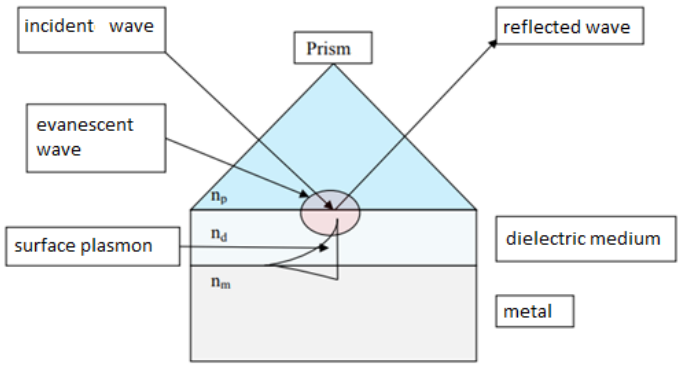

Figure 6 : Excitation of a surface plasmon in the Otto device.

I.3.1.2 Coupling of a surface plasmon by a diffraction grating:

Another solution to couple a light wave to a surface plasmon is to use the evanescent order diffraction of a diffraction grating, which will satisfy the equality of equation (Eq.I. 18). Suppose a metallic sinusoidal network of semi-infinite layer of permittivity constant εm in a dielectric medium of permittivity ε_d as shown schematically in Figure 7.

We consider a polarized incident wave TM (Transverse Magnetic), thus presenting the component of the magnetic field normal to the plane of incidence and parallel to the lines of network.

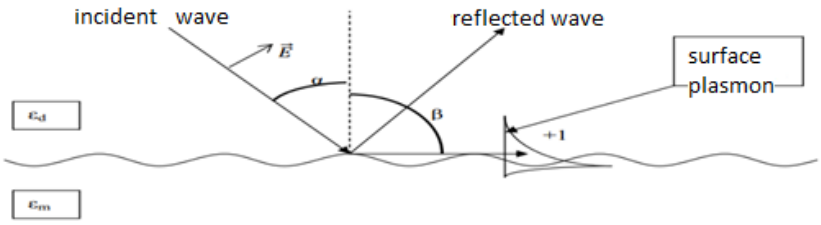

Figure 7 : Excitation of a surface plasmon by a diffraction grating, with the diffractive order +1.

There are then orders of diffraction subject to the equation :

$$m\lambda = \Lambda\big(sin(\alpha) + sin(\beta)\big) \qquad \textbf{Eq.I. 23}$$

With λ the incident wave, m the diffraction order, Λ the pitch of the grating, α the angle of incidence with respect to the normal to the grating and β the angle of the diffracted order from the normal to the network. For an order to be evanescent it is necessary that β = 90 . either :

$$sin(\alpha) = \frac{m\lambda}{\Lambda} 1 \qquad \textbf{Eq.I. 24}$$

with the ± sign depending on the positive or negative order .

If we fulfill this first condition, it then appears that the diffracted wave in the evanescent order must satisfy equality (Eq.I. 18), that is to say that it can couple a surface plasmon.

In a schematic and simplified way, this condition can be illustrated graphically, in the reciprocal space of the wave vectors, by a simple vector construction also called Ewald circle.

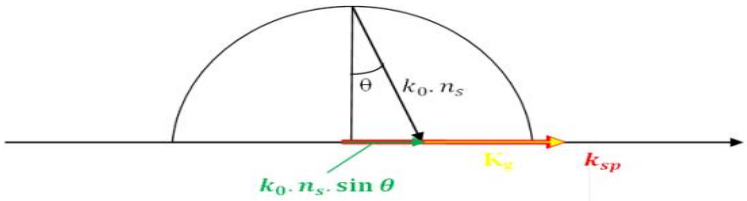

Figure 8 : Representation of the coupling in reciprocal space of the wave vectors.

By referring to the reciprocal space of vectors (see Figure 8) we can write

the following equation:

$$k_{sp} = k_0 n_s sin(\theta) + nk_g \qquad \textbf{Eq.I. 25}$$

With n the diffraction order, we see that the wave vector of the grating becomes an adjustment variable such as the parameter A of equation (Eq.I. 21). As we were able to present it previously with the coupling devices via a prism, where a maximum plasmonic excitation is reached for a given metal thickness; the same is true for networks but with the network depth parameter h. Let us take as an example a grating of period with a sinusoidal profile structuring a gold layer at an interface with air (see Figure 9).

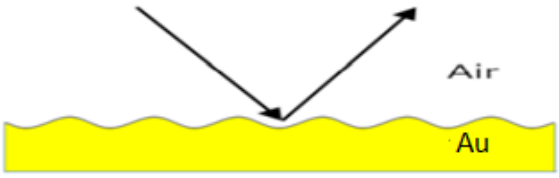

Figure 9 : Network diagram of a grating Gold-Air interface

To observe the phenomenon, we are looking for the minimum of the spectrum reflected by an angular scan which will then be the response to an excitation of a surface plasmon mode by energy transfer. The Figure 10 below represents a digital simulation of an angular scan at different grating depth.

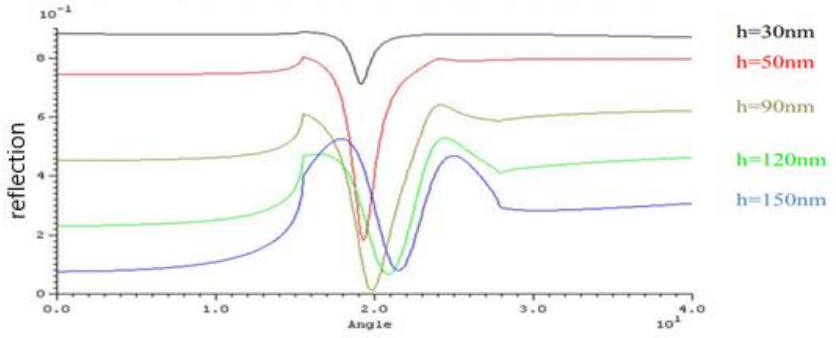

Figure 10 : Variation of reflected intensity as a function of angle of incidence. On the abscissa the angles from 0 ° to 40 °, on the ordinate the reflected relative intensity. On the graph: in black h = depth of the network [22].

We see in Figure 10 a minimum reflected intensity for a depth q = 90 nm. This minimum intensity then corresponds to the maximum coupling between the plasmon and the incident wave. The angular displacement of the peak is explained by a variation in the effective index of the surface plasmon as a function of the depth. Finally, the more the depth increases, the more we tend to observe an increase in the width of the resonance peak (in Figure 10 we note a large difference in peak width if we observe the black curve h = 30 nm and the blue curve h = 150nm). The exaltation factor quantifies the coupling and synchronism between the plasmon mode and the incident wave, it is described by [23]:

$$T^{el} = \frac{2\left|\varepsilon_m^{'}\right| cos(\theta_0)(1-R)}{\varepsilon_m^{''}(|\varepsilon_m^{'}|-1)^{1/2}} \qquad \textbf{Eq.I. 26}$$

With T the exaltation factor of the electromagnetic field, R the reflection coefficient and cos (θ_0) which can be obtained with the following relation:...

$$sin(\theta_0) = \left(\frac{\varepsilon_m^{'}}{\varepsilon_m^{'}} + 1\right)^{1/2} - \frac{\lambda}{\Lambda} \qquad \textbf{Eq.I. 27}$$

The factor being maximum with R = 0, that is to say with a minimum reflection. Thanks to this, we note the dependence of the coupling factor on the wavelength. Thus for a network of 800 nm with a pitch at an Air-Silver interface, the factor T^{el}= 124 for λ = 650 nm and T^{el}= 27 for λ=420nm.

I.4 Surface Plasmon Resonance:

This is an example where the surface plasmon can be excited by the evanescent wave and this phenomenon is called surface plasmon resonance (SPR). When this happens, the intensity of the reflected light decreases sharply. The decays of the excited surface plasmon include energy conversion to phonons or photons. One requirement for the SPR is that k_{SPP} equals to k_{photon} :

$$\theta_{SPR} = \sin^{-1}\left(\frac{1}{n_1}\sqrt{\frac{n_2^2 n_m^2}{n_2^2 + n_g^2}}\right) \qquad \textbf{Eq.I.28}$$

The angle required for the resonance, θ_{SPR}, is related to n_2 when n_1 and n_g are fixed. Adsorption and desorption on the gold surface (for example Figure 4) changes the refractive index of media 2 near the metal–dielectric interface and the resonance angle changes accordingly. Therefore, the monitoring of the θ_{SPR} change can be used to analyze the adsorption–desorption or association–dissociation activities that take place on the gold surface.

I.5 Skin depth and electric field extension of the surface plasmon:

I.5.1 Skin depth:

The electric field Ez of the plasmon decreases exponentially in both media such as :

$E_z = e^{-(|k_{zi}||z|)}$. The skin depth corresponds to the depth (z) in a material for which the modulus of the electric field is attenuated by $\frac{1}{e}$ This skin depth then defines the maximum penetration of the Ez field into one of the substrates. So we can define in each of the two media the depth of skin such that

In the dielectric:

$$Z_d = \frac{\lambda}{2\pi}\left(\frac{\varepsilon_m' + \varepsilon_d}{\varepsilon_d^2}\right)^{1/2} \qquad \textbf{Eq.I. 29}$$

In the metal:

$$Z_m = \frac{\lambda}{2\pi}\left(\frac{\varepsilon_m' + \varepsilon_d}{\varepsilon_m'^2}\right)^{1/2} \qquad \textbf{Eq.I. 30}$$

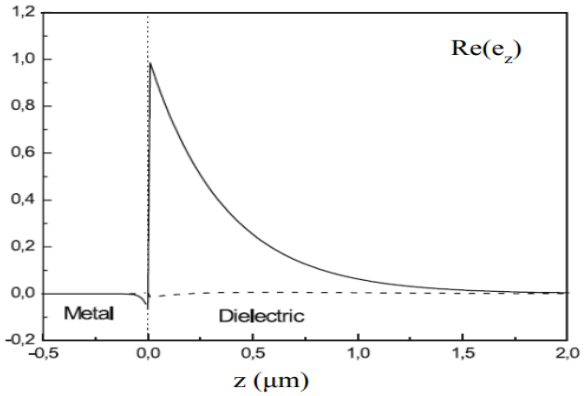

Figure 11 : Schematic of the propagation of the electric field Ez along the z axis for a gold interface and a dielectric of index 1.32 for a wavelength of 800 nm. [19]

By observing Figure 11, we can clearly see this asymmetry in the distribution of the Ez field. Likewise, the variation in the excitatory wavelength makes it possible to vary the depth of the skin (see Figure 12).

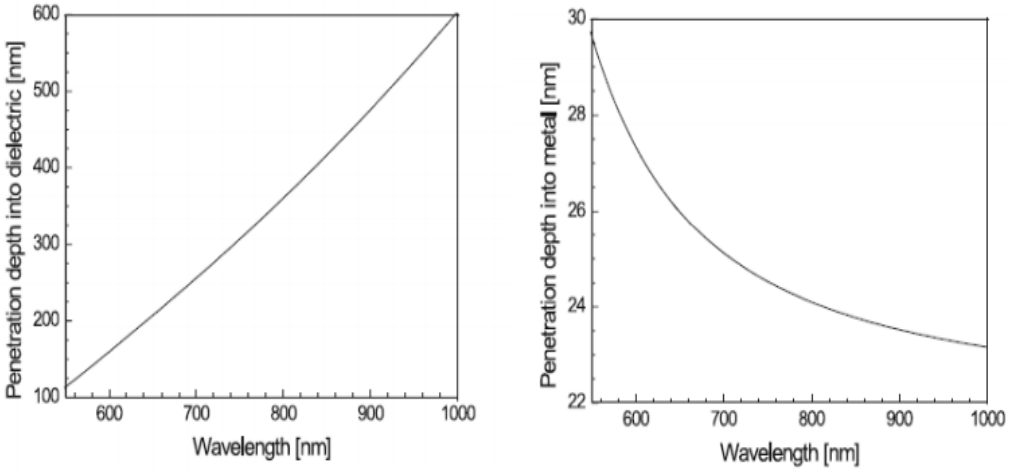

Figure 12 : Skin depth as a function of wavelength at a gold and dielectric interface (index n = 1.32). Left graphic in dielectric, right graphic in metal.

The wavelength dependence of Zd and Zm is different. It increases in the case of the dielectric and decreases in the metal as the wavelength increases, this is entirely due to the denominator in the expression of skin depth. In the case of the dielectric, the permittivity is low and fluctuates little, in the case of metal the real permittivity is high and fluctuates. This then causes the difference in behavior.

I.5.2 Surface plasmon propagation length:

The attenuation is used to define the propagation length of the surface plasmon L which is defined as the distance at which the intensity of the surface plasmon decreased to $\frac{1}{e}$ by:

$$L = 1(2k_x'') \qquad \textbf{Eq.I. 31}$$

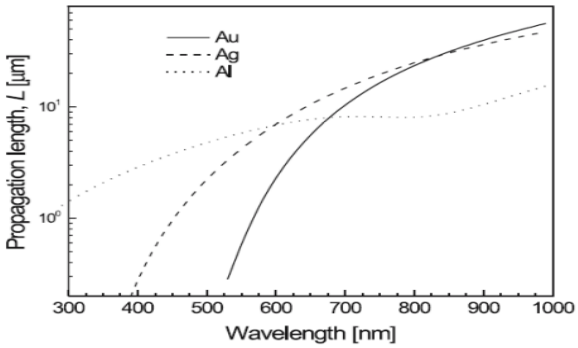

Figure 13 : Graph showing the propagation length of the surface plasmon at the interface of a metal and a dielectric (n = 1.32) as a function of three metals (gold: Au, silver: Ag and aluminum: Al) and wavelength.

I.6 Surface plasmon mode: Long Range Plasmon Mode and Short Range Plasmon Mode :

These modes exist for a fine metal thickness on the order of twice the skin depth of a standard surface plasmon. In this case, a surface plasmon at one interface can no longer be described without taking into account the interactions at the other interface. Suppose a dielectric-metal-dielectric structure, with ε_1 the permittivity of the first dielectric, εm the permittivity of the metal and ε_2 the permittivity of the second dielectric in addition, the electric field Ez passes through zero at the center of the metal, thus allowing much lower losses than a surface plasmon on a single interface (as illustrated by Figure 14). This mode is called Long Range Plasmon Mode (LRPM). The even mode for its part presents a confinement mainly in the metal leading to much more losses.

This mode is called Short Range Plasmon Mode (SRPM). These significant losses make the SRPM less interesting compared to the LRPM for the propagation of modes.

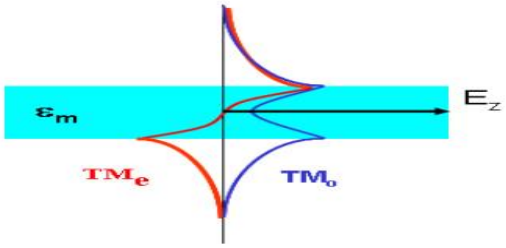

Figure 14 : The electric fields E_z of LRPM and SRPM for a layer of metal of permittivity ε_m encapsulated in a dielectric. With TM_e the electric field E_z of the LRPM and TM_0 the electric field E_z of the SRPM. [24]

The table below shows the propagation characteristics of a surface plasmon and an LRPM for the same excitatory wavelength:

Mode	N_{eff}-n_1	Attenuation (dB/mm)	Propagation length (µm)	Mode width (µm)
SPP	0.013	44	98	1.27
Long Range Mode Plasmon	0.0023	1.2	3776	6.12

Table I.1 The modal properties of surface plasmon (SPP) and Long Range Mode (LRPM) plasmon.

With λ = 1550 nm, the metal is silver and the dielectric is quartz with for the structure of the long range mode a metal thickness of t = 20 nm, n_1 the index of the dielectric and n_{eff} the effective index of the plasmon surface or long range mode. [26]

I.7 Surface plasmons waveguides:

The propagation of plasmons on an interface can be managed by locally modifying the surface, via roughness or a network of nanomaterials. As a result, it is possible to create conventional optical elements such as lenses or plasmonic mirrors.

We will see a particular confinement of the plasmon on a very thin metal strip (we can compare this to a plasmonic "optical fiber") which makes it possible to guide the plasmons over large distances.

I.7.1 Plasmon waveguide on a flat surface:

Control of the direction of propagation of a plasmon at a metal-dielectric interface can be achieved by including on the propagation interface defects capable of redirecting the plasmon. These can be periodic or aperiodic surface undulations, as well as nanoscale holes perforating the metal surface. The precise management of these defects allows the creation of functional elements such as Bragg mirrors to reflect the plasmon or focal elements, that is to say plasmonic lenses. These two elements offer the possibility of creating guiding circuits, focusing a surface wave such as the plasmon.

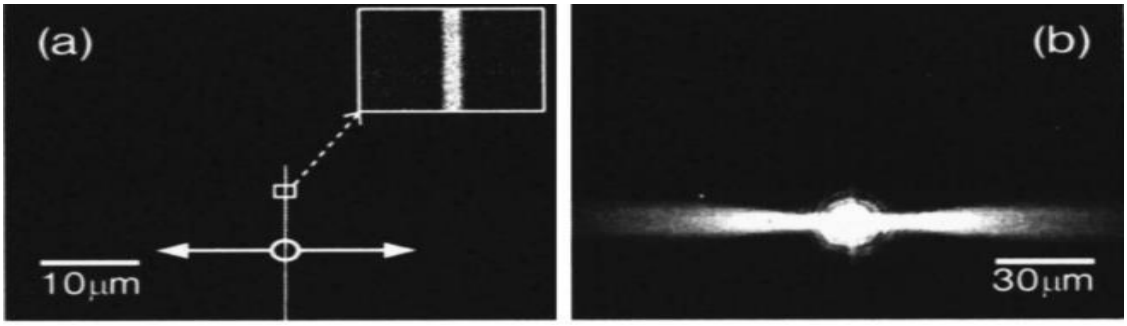

Figure 15 : (a) SEM (scanning electron microscopy) image of the gold line of dimension 70nm×160nm×20µm and of the array of nanodots with a radius of 140 nm, each row of nanopots is spaced of 350 nm. In the square at the top right is a zoom × 12 centered on the network of nano plots. The circle and the double arrows correspond respectively to the focal point of the LASER and to the direction of propagation of the plasmon. (b) The image of the corresponding UV fluorescence shows that the plasmon propagating in the direction of the nanopots is reflected.

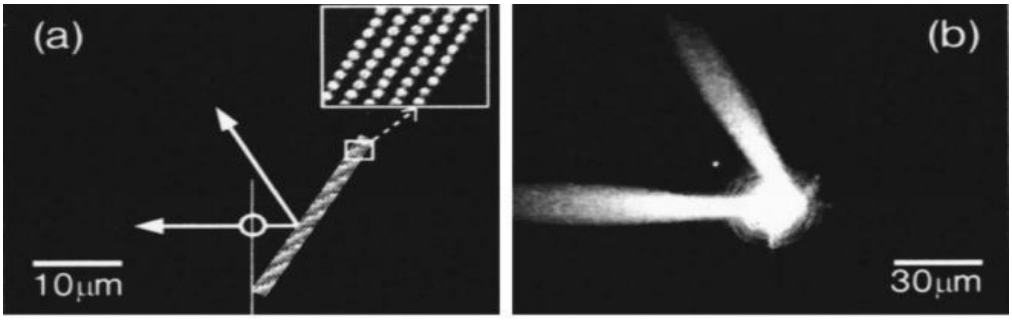

Figure 16 : (a) SEM (scanning electron microscopy) image of the gold line of dimensions 70nm×160nm×20µm. In the square at the top right is a zoom ×12 centered on the line. The circle and the double arrows correspond respectively to the point of focus of the laser and the direction of propagation of the plasmon. (b) The corresponding UV fluorescence image, this clearly shows the propagation of the surface plasmon.

I.7.2 Metal/Deilectric Waveguides:

This section presents the electromagnetic theory of optical waveguides based on Maxwell's equations using modal method In this approach, the electric and magnetic field vectors E and H are each expressed as a sum of field contributions, one part representing power that is guided along the waveguide, the remaining part representing power that is radiated from the waveguide [19]:

$$E(r,t) = E_G(r,t) + E_R(r,t), \quad \textbf{Eq.I.32}$$

$$H(r,t) = H_G(r,t) + H_R(r,t), \quad \textbf{Eq.I.33}$$

Where subscript G and R denote the guided and radiation fields, r is space vector and t is time. The guided, or bound, portion can be expressed as a finite sum of guided modes:

$$E_G(r,t) = \sum_j \alpha_j E_j(r,t), \quad \textbf{Eq.I.34}$$

$$H_G(r,t) = \sum_j \alpha_j H_j(r,t), \quad \textbf{Eq.I.35}$$

Where j is a mode number (j=1,2,...,M) and α_j are modal amplitudes. The modal fields $E_j(r,t)$ and $H_j(r,t)$ are solutions to source-free Maxwell equations:

$$\nabla \times E(r,t) + \mu \frac{\partial H(r,t)}{\partial t} = 0, \quad \textbf{Eq.I.36}$$

$$\nabla \cdot (\mu H(r,t)) = 0, \quad \textbf{Eq.I.37}$$

$$\nabla \times H(r,t) - \varepsilon 0 \varepsilon(r) \frac{\partial E(r,t)}{\partial t} = 0, \quad \textbf{Eq.I.38}$$

$$\nabla \cdot (\varepsilon_0 \varepsilon(r) E(r,t)) = 0, \quad \textbf{Eq.I.39}$$

Where μ is magnetic permeability, ε is relative permittivity (dielectric constant) of the medium, and ε 0is the free-space permittivity. For non-magnetic materials, which commonly constitute an optical waveguide, the magnetic permeability μ is equal to the free-space permeability μ0.Assuming a wave-guide consisting of linear isotropic media, we can reduce Maxwell's (Eq.I.36-Eq.I.39)to the vector wave equations:

$$\Delta E(r,t) - \varepsilon_0\varepsilon(r)\mu_0 \frac{\partial^2 E(r,t)}{\partial t^2} = \nabla\big(E(r,t)\cdot\nabla \ln\varepsilon_0\varepsilon(r)\big) \qquad \textbf{Eq.I.40}$$

$$\Delta H(r,t) - \varepsilon_0\varepsilon(r)\mu_0 \frac{\partial^2 H(r,t)}{\partial t^2} = (\nabla\times H)\times(\nabla \ln\varepsilon_0\varepsilon(r)), \qquad \textbf{Eq.I.41}$$

Where the vector differential operators ∇ and Δ are defined as follows:

$$\nabla f = \frac{\delta f}{\delta x}x_0 + \frac{\delta f}{\delta y}y_0 + \frac{\delta f}{\delta z}z_0 \qquad \textbf{Eq.I.42}$$

$$\nabla\cdot A = \frac{\delta Ax}{\delta x} + \frac{\delta Ay}{\delta y} + \frac{\delta Az}{\delta z} \qquad \textbf{Eq.I.43}$$

$$\nabla\times A = \left(\frac{\delta A_y}{\delta z} - \frac{\delta A_z}{\delta y}\right)x_0 + \left(\frac{\delta A_z}{\delta x} - \frac{\delta A_x}{\delta z}\right)y_0 + \left(\frac{\delta A_x}{\delta y} - \frac{\delta A_y}{\delta x}\right)z_0 \qquad \textbf{Eq.I.44}$$

$$\Delta A = \left(\frac{\partial^2 A_x}{\partial x^2} + \frac{\partial^2 A_x}{\partial y^2} + \frac{\partial^2 A_x}{\partial z^2}\right)x_0 + \left(\frac{\partial^2 A_y}{\partial x^2} + \frac{\partial^2 A_y}{\partial y^2} + \frac{\partial^2 A_y}{\partial z^2}\right)y_0 + \left(\frac{\partial^2 A_z}{\partial x^2} + \frac{\partial^2 A_z}{\partial y^2} + \frac{\partial^2 A_z}{\partial z^2}\right)z_0 \qquad \textbf{Eq.I.45}$$

And f and A = (A_x, A_y, A_z) are scalar and vector functions on Cartesian coordinates (x,y,z) and x_0,y_0 and z_0 are unit vectors. If we assume translational invariance of the waveguide in the z-direction, propagation along the z-direction, and time dependence of the field vectors in the form of exp(– iωt), where ω is the angular frequency and $i = \sqrt{-1}$, the modal fields can be expressed in the separable form:

$$E = e(x,y)\exp(i(\beta z - \omega t)) = \{e_t(x,y) + e_z(x,y)z_0\}\exp(i(\beta z - \omega t)) \qquad \textbf{Eq.I.46}$$

$$H = h(x,y)\exp(i(\beta z - \omega t)) = \{h_t(x,y) + h_z(x,y)z_0\}\exp(i(\beta z - \omega t)) \qquad \textbf{Eq.I.47}$$

Where β denotes the propagation constant of a mode and subscript t denotes the transversal component of field vectors. For the modal fields described by Eq.I.46 and Eq.I.47, the vector wave equations can be reduced to:

$$\{\Delta_t + \omega^2\varepsilon\varepsilon_0\mu_0 - \beta^2\}e = -\{\nabla_t + i\beta z\}\{e_t\,\nabla_t \ln\varepsilon\varepsilon_0\} \qquad \textbf{Eq.I.48}$$

$$\{\Delta_t + \omega^2\varepsilon\varepsilon_0\mu_0 - \beta^2\}h = -(\nabla_t \ln\varepsilon\varepsilon_0)\times(\{\nabla_t + i\beta z\}\times h) \qquad \textbf{Eq.I.49}$$

These vector wave equations are a restatement of Maxwell's equations for an arbitrary refractive index profile. Subject to the requirements that the modal fields are bounded everywhere and decay sufficiently fast at large distances from the waveguide, these equations contain all of the information necessary to determine the modal fields and propagation constants of all the guided modes of the wave guide. Let us consider an optical waveguide consisting of three homogeneous media (figure3) with a permittivity profile:

$$\varepsilon(x) = \varepsilon 3 = n_3^2, \qquad x > d \qquad \textbf{Eq.I.50}$$

$$\varepsilon(x) = \varepsilon 2 = n_2^2, \qquad -d \le x \le d \qquad \textbf{Eq.I.51}$$

$$\varepsilon(x) = \varepsilon 1 = n_1^2, \qquad x < -d \qquad \textbf{Eq.I.52}$$

where d is the waveguiding layer half-width and εi and ni(i=1,2,3) are generally complex permittivities and refractive indices (hereafter, we shall be using ε for the relative permittivity unless stated otherwise).By orienting Cartesian axes as shown in Fig. 1, the field vectors depend on x and z only and Eq.I.46 and Eq.I.47 can be written as:

$$E = e(x)\exp(i(\beta z - \omega t)) \qquad \textbf{Eq.I.53}$$

$$H = h(x)\exp(i(\beta z - \omega t) \qquad \textbf{Eq.I.54}$$

In each medium the $\nabla_t \ln\varepsilon$ term vanishes and each Cartesian field component satisfies a simplified wave equation:

$$\{\Delta_t + \omega^2 \varepsilon \varepsilon_0 \mu_0 - \beta^2\} e_i = 0 \qquad \textbf{Eq.I.55}$$

$$\{\Delta_t + \omega^2 \varepsilon \varepsilon_0 \mu_0 - \beta^2\} h_i = 0 \qquad \textbf{Eq.I.56}$$

Where i=x,y,z.

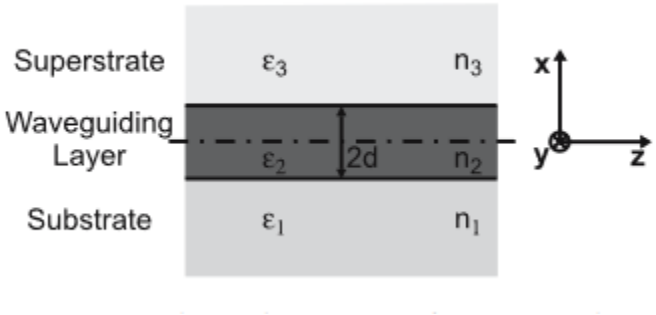

Figure 17 : Section of a planar waveguide with a step refractive index profile.

The solution of Eq.I.55 and Eq.I.56 yields two linearly independent sets of modes. One set with $h_z = 0$ everywhere, referred as to transverse magnetic(TM); the other with $e_z = 0$ everywhere, referred as to transverse electric (TE).Substitution of the field profiles Eq.I.53 and Eq.I.54 into Eq.I.55 and Eq.I.56, respectively, yields for the transversal components of the field vectors:

$$\frac{\partial^2 e_y(x)}{\partial x^2} + \left(\omega^2 \varepsilon \varepsilon_0 \mu_0 - \beta^2\right) e_y(x) = 0; \quad \text{for the TE modes} \qquad \textbf{Eq.I.57}$$

$$\frac{\partial^2 h_y(x)}{\partial x^2} + \left(\omega^2 \varepsilon \varepsilon_0 \mu_0 - \beta^2\right) h_y(x) = 0; \quad \text{for the TM modes} \qquad \textbf{Eq.I.58}$$

In each medium the solution of wave Eq.I.57 and Eq.I.58 can be expressed as a linear combination of functions: $\exp(i\kappa_i x)$ and $\exp(-i\kappa_i x)$, where $\kappa_i^2 = \omega^2 \varepsilon_i \varepsilon_0 \mu_0 - \beta^2$ $(i = 1, 2, 3)$. The other non-zero components of the field vectors can be determined from Eq.I.36 and Eq.I.38. This yields:

TE modes:

$$e_y(x) = a_i^+ \exp(i\kappa_i x) + a_i^- \exp(-i\kappa_i x) \qquad \textbf{Eq.I.59}$$

$$h_x(x) = \frac{\beta}{\mu_0 \omega} \left[a_i^+ \exp(i\kappa_i x) + a_i^- \exp(-i\kappa_i x)\right] \qquad \textbf{Eq.I.60}$$

$$h_z(x) = -\frac{\kappa_i}{\mu_0 \omega} \left[a_i^+ \exp(i\kappa_i x) - a_i^- \exp(-i\kappa_i x)\right. \qquad \textbf{Eq.I.61}$$

TM modes :

$$h_y(x) = b_i^+ \exp(i\kappa_i x) + b_i^- \exp(-i\kappa_i x) \quad \textbf{Eq.I.62}$$

$$e_x(x) = -\frac{\beta}{\varepsilon_i \varepsilon_0 \omega}[b_i^+ \exp(i\kappa_i x) + b_i^- \exp(-i\kappa_i x)] \quad \textbf{Eq.I.63}$$

$$e_z(x) = \frac{\kappa_i}{\varepsilon_i \varepsilon_0 \omega}[b_i^+ \exp(i\kappa_i x) - b_i^- \exp(-i\kappa_i x) \quad \textbf{Eq.I.64}$$

Outside the waveguiding layer, modal fields bound to the waveguide are described by only one of these solutions and decay exponentially with an increasing distance from the waveguide. Consequently, in each pair of amplitudes a_i^+ and $a_1^+$and a_2^+ and a_3^+, one amplitude is equal to zero for TE modes ,and in each pair of amplitudes b_i^+ and b_1^+ and b_2^+ and b_3^+, one amplitude is equal to zero for TM modes. The boundary conditions of Maxwell's equations require that the components of the electric and magnetic field intensity vectors parallel to the boundaries of the waveguiding layer are continuous at the boundaries (x=d and x=–d). These boundary conditions present a homogenous series of four linear equations for four unknown amplitudes, which yields a non-zero solution only if the determinant of the matrix of co-efficients is equal to zero. This requirement leads to the eigenvalue equations:

$$\tan(\kappa d) = \frac{\frac{\gamma_1}{\kappa} + \frac{\gamma_3}{\kappa}}{1 - \left(\frac{\gamma_1}{\kappa}\right)\left(\frac{\gamma_3}{\kappa}\right)} \text{ ; for the TE mode} \quad \textbf{Eq.I.65}$$

$$\tan(\kappa d) = \frac{\frac{\gamma_1 \varepsilon_2}{\kappa \varepsilon_1} + \frac{\gamma_3 \varepsilon_2}{\kappa \varepsilon_3}}{1 - \left(\frac{\gamma_1 \varepsilon_2}{\kappa \varepsilon_1}\right)\left(\frac{\gamma_3 \varepsilon_2}{\kappa \varepsilon_3}\right)} \text{ ; for the TM mode} \quad \textbf{Eq.I.66}$$

Where: $\kappa^2 = \omega^2 \varepsilon_2 \varepsilon_0 \mu_0 - \beta^2$ and $\gamma_{1,3}^2 = \beta^2 - \omega^2 \varepsilon_{1,3} \varepsilon_0 \mu_0$.

The eigenvalue Eq.I.65 and Eq.I.66 are transcendental equations for unknown modal propagation constants. After solving the eigenvalue equations, the field profiles can be determined by substituting the values of modal propagation constants β into the boundary conditions and calculating the amplitudes a_i^+ and a_i^- for TE modes and b_i^+ and b_i^- for TM modes (i=1,2,3). If the media constituting the waveguide are lossless (ε1, ε2, and ε3 are real positive numbers), the propagation constants are also real. Propagation constants of modes of a waveguide containing

absorbing media (e.g., metal) are complex. The propagation constant is related to the modal effective index n_{ef} and modal attenuation b as follows:

$$n_{ef} = \frac{c}{\omega}\mathrm{Re}\{\beta\} \quad \textbf{Eq.I.67}$$

$$b = \mathrm{Im}\{\beta\}\frac{0.2}{\ln 10} \quad \textbf{Eq.I.68}$$

Where Re{} and Im{} denote the real and imaginary parts of a complex number, respectively, and c denotes the speed of light in vacuum; the modal attenuation b is in dB cm^{-1} if β is given in m^{-1}.

I.7.3 MIM waveguides:

Considering a TM mode ($E_y = 0, H_x = H_z = 0$)propagating in the +z direction in a MIM structure shown in Figure 18, the magnetic fields in the regions can be represented by:

$$H_y = A_1\exp(\kappa_m x) \quad \textbf{Eq.I.69}$$

$$H_y = B_1\exp(\kappa_d x) + B_2\exp(-k_d x) \quad \textbf{Eq.I.70}$$

$$H_y = A_2\exp(-\kappa_m x) \quad \textbf{Eq.I.71}$$

Where $\kappa_m = \left(\beta^2 - k_0^2\varepsilon_m\right)^{1/2}$ and $\kappa_d = (\beta^2 - k_0^2\varepsilon_d)^{1/2}$are the complex wave vectors in the +x direction in the metal and dielectric, with β being the propagation constant in +z direction and $k_0 \equiv \lambda/2\pi$ being the freespace wavevector magnitude; the A's and B's are unknown constants to be determined by solving the boundary condition equations. It is assumed that both the dielectric and the metal are lossless, that is, both ε_d and $\varepsilon_m$are realwith ε_d being positive and $\varepsilon_m$being negative. Also it is noted that the values of κ_d can be either real or imaginary, which correspond to plasmonic modes or oscillatory modes, respectively [20]. By using Maxwell's curl of H equation $\nabla \times \vec{H} = \frac{\partial \vec{D}}{\partial t}$, the tangential electric field (E_z) can be:

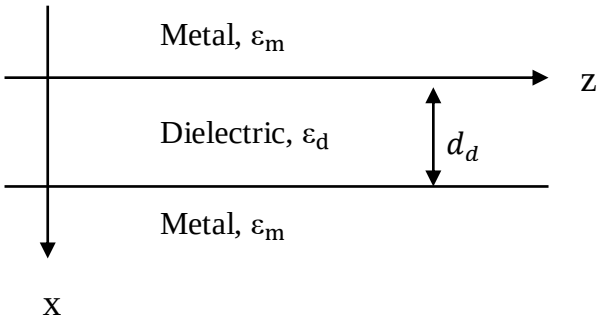

Figure 18 : Configuration and coordinate system of a metal-insulator-metal (MIM) structure. The structure is invariant in the y direction.

Represented as

$$E_z = \frac{1}{j\omega\varepsilon}\frac{\partial H_y}{\partial x} \qquad \textbf{Eq.I.72}$$

The tangential electric fields in each of the three regions of the MIM structure are:

$$\mathrm{E_z} = \frac{\mathrm{k_m}}{\mathrm{j\varepsilon_0\varepsilon_m}}\mathrm{A_1}\exp(\kappa_\mathrm{m}\mathrm{x}) \qquad \textbf{Eq.I.73}$$

$$\mathrm{E_z} = \frac{\mathrm{k_d}}{\mathrm{j\omega\varepsilon_0\varepsilon_d}}[\mathrm{B_1}\exp(\kappa_\mathrm{d}\mathrm{x}) + \mathrm{B_2}\exp(-\mathrm{k_d}\mathrm{x})] \qquad \textbf{Eq.I.74}$$

$$\mathrm{E_z} = -\frac{\mathrm{k_m}}{\mathrm{j\omega\varepsilon_0\varepsilon_m}}\mathrm{A_2}\exp(-\kappa_\mathrm{m}\mathrm{x}) \qquad \textbf{Eq.I.75}$$

To satisfy the boundary conditions at x=0 and x=$\mathrm{d_d}$, $\mathrm{E_z}$ and $\mathrm{H_y}$ must be continuous at both interfaces. In brief, there are four equations of boundary conditions and five unknowns ($\mathrm{A_1}, \mathrm{A_2}, \mathrm{B_1}, \mathrm{B_2}$, and β). Therefore, by algebraic manipulation, for real $\mathrm{k_d}$the characteristic equation for β is given a:

$$\tanh(k_d d_d) = -\frac{2}{\left(\frac{\varepsilon_m}{k_d}\frac{\varepsilon_d}{\varepsilon_m} + \frac{k_d}{k_m}\frac{\varepsilon_m}{\varepsilon_d}\right)} \qquad \textbf{Eq.I.76}$$

Recalling the hyperbolic function identity

$$\tanh(\theta) \equiv -\frac{2}{\tanh\frac{\theta}{2} + \coth\frac{\theta}{2}} \qquad \textbf{Eq.I.77}$$

We have two possibilities, the first is:

$$\tanh\left(\frac{k_d d_d}{2}\right) = -\frac{k_m}{k_d}\frac{\varepsilon_d}{\varepsilon_m} \qquad \textbf{Eq.I.78}$$

And the other possibility is:

$$\tanh\left(\frac{k_d d_d}{2}\right) = -\frac{k_d}{k_m}\frac{\varepsilon_m}{\varepsilon_d} \qquad \textbf{Eq.I.79}$$

The first possibility corresponds to the TM_0 plasmonic mode, which has symmetric mode profile in H_y and the field component are evanescent (i.e k_d is real) in the dielectric core. It is a plasmonic mode for all values of β. The second possibility corresponds to TM_1 plasmonic mode, which has odd symmetry in H_y. It is a plasmonic mode for sufficiently large values of β , but an oscillatory mode (i.e. k_d is imaginary and the field components in the dielectric are sinusoidal) for small values β. There is a smooth transition from an oscillatory mode at low frequencies to an evanescent mode at higher frequencies. The transition occurs at the light line of the dielectric. The characteristic equations for the TM oscillatory modes (imaginary k_d) can be obtained in a similar way as their plasmonic counterparts, yielding:

$$\tan\left(\frac{k_d d_d}{2}\right) = -\frac{k_m}{k_d}\frac{\varepsilon_d}{\varepsilon_m} \qquad \textbf{Eq.I.80}$$

And

$$\tan\left(\frac{k_d d_d}{2}\right) = -\frac{k_d}{k_m}\frac{\varepsilon_m}{\varepsilon_d} \qquad \textbf{Eq.I.81}$$

Where $k_d = (k_0^2\varepsilon_d - \beta^2)^{1/2} = -jk_d$, is the wave vector in +x direction in the dielectric.

Equation 2.3 corresponds to symmetric oscillatory $TM_2, TM_4, TM_6\ldots$ modes, while Eq.I.81 corresponds to asymmetric oscillatory $TM_1, TM_3, TM_5,\ldots$modes.

Also, TE modes may exist in a MIM structure as shown in Figure 18 Following a similar approach as for the TM modes, the characteristic equations for the TE modes are given as:

$$\tan\left(\frac{k_d d_d}{2}\right) = -\frac{k_m}{k_d} \qquad \textbf{Eq.I.82}$$

And

$$\tan\left(\frac{k_d d_d}{2}\right) = -\frac{k_d}{k_m} \qquad \textbf{Eq.I.83}$$

Eq.I.82 corresponds to symmetric oscillatory TE_0 ,TE_2, TE_4,…modes, while Eq.I.83 corresponds to asymmetric oscillatory TE_1, TE_3, TE_5,…modes.

The dispersion relation for the TM and TE modes in a MIM structure can be further analyzed by considering the frequency dependence of ε_d and ε_m [21]. The ε_d is a constant and

$\varepsilon_m = 1 - {\omega_p^2}/{\omega^2}$ (Drude free-electron-gas model) is the same as the assumption for the SP mode at a single metal/dielectric interface.

I.8 Conclusion:

Along this chapter we presented the basic fundamentals and notions about surface plasmons and the related equations, parameters and the properties of the SP's at a single metal/dielectric interface and TM and TE modes in a MIM waveguide were discussed and because of the superior lateral confinement and slow-wave property, MIM-based devices and interconnects offer a remarkable potential for realizing integrated sensors.

Chapter II: Plasmonic sensors

II.1 Introduction:

Sensors in general and specifically temperature sensors are being utilized in many fields from chemical and biological, to industrial applications.

In the previous chapter we have presented fundamentals of the theory of plasmonics in general and interestingly the phenomenon of surface plasmons and it was shown that the propagation constant of surface plasmons depends greatly on the refractive index at the surface of a metal film supporting the surface plasmon. Within this chapter we shall introduce how this phenomenon can be used to make sensors, The concept of sensors based on surface plasmons, commonly referred as to surface plasmon resonance (SPR) sensors, is described and the main approaches to SPR sensing are presented along with the particular case of MIM based temperature sensor. In addition, the conception and modeling methods of these sensors is introduced and the main performance characteristics are defined.

II.2 Plasmonic sensing mechanisms:

There are two fundamental excitations of plasmons [29]: SPPs and LSPRs. SPPs are waves propagating along a metal–dielectric interface, and LSPRs are non-propagating excitations of the conduction electrons of metallic nanostructures coupled to the electromagnetic field of the incident light. The excitation conditions of these two types both depend on the dielectric medium surrounding the metal. This property lays the foundation for plasmonic sensing. When the target analyte is bound onto the metal the dielectric environment changes, which modifies the plasmon excitation condition. The change of excitation condition is then measured. The resulting output is a measurement of the concentration of the analyte.

II.2.1 Resonance conditions for sensing:

For an SPP propagating along the interface of the metal and dielectric, the dispersion relation is:

$$\beta = k_0 \sqrt{\frac{\varepsilon_m \varepsilon_d}{\varepsilon_m + \varepsilon_d}} \qquad \textbf{Eq.II. 84}$$

Where β is the propagating constant of the SPP which corresponds to the component of the SPP's wavevector along the propagating direction, $k_0 = \omega/c$ is the wavevector of the propagating wave in vacuum, $\varepsilon_m(\omega)$ is the dielectric function of the metal with ω the angular frequency, and $\varepsilon_d = n^2$

is the dielectric constant of the dielectric environment with *n* the refractive index. The intrinsic sensitivity of SPP-based sensors is defined as [2]

$$S_{SPP}^{int} = \frac{\partial Re\{\beta\}}{\partial n} \qquad \textbf{Eq.II. 85}$$

Which is the sensitivity of the SPP's propagating constant to the change in refractive index. This S^{int}_{SPP} is influenced by the interaction volume between the SPP wave and the analyte layer (which causes the refractive-index change) [30].

II.2.2 Plasmonic sensor detection principle:

A light wave is beamed onto a coupler, in our case metallic nanostructures, which makes it possible to excite the surface plasmons, and the transmitted signal then makes it possible to follow, thanks to the plasmonic resonance, the evolution of the quantity to be measured.

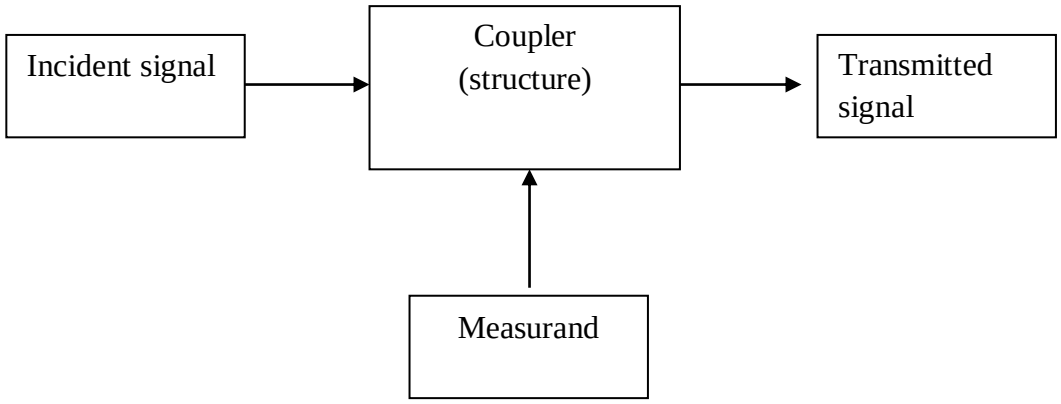

Figure II.19 an SPR sensor functioning principle.

At the coupler level, we have two choices: either a planar structure, with prism coupling, this is the preferred technique in commercial systems already available (Biacore, IBIS, Genoptics ...) focused primarily on the biosensor, a coupling system with nanoarrays. It is this last type of coupling that will interest us in the following, especially since it allows a miniaturization of such sensors, an aspect that is much more difficult to achieve with a planar structure.

The observed signal then depends on how we follow the evolution of the transmission spectrum:
-Transmission peak tracking: In this method, the transmission peak wavelength, which shifts with the change in refractive index, is the measurand. This method assumes that the transmitted signal is analyzed by a spectrometer, so it is not necessarily indicated for the purpose of miniaturization of the sensor.

-Intensity / phase transmitted at a fixed wavelength: by illuminating the sensor with monochromatic light of a very specific wavelength, then the displacement of the transmission peak will result in a variation of the intensity, or of the phase depending of the monitored quantity, of the transmitted signal. This method makes it easier to design miniaturized sensors. The rest of the study will focus more particularly on this operating principle, with monitoring of the transmitted intensity.

The previous two methods of measuring are described in the following figure:

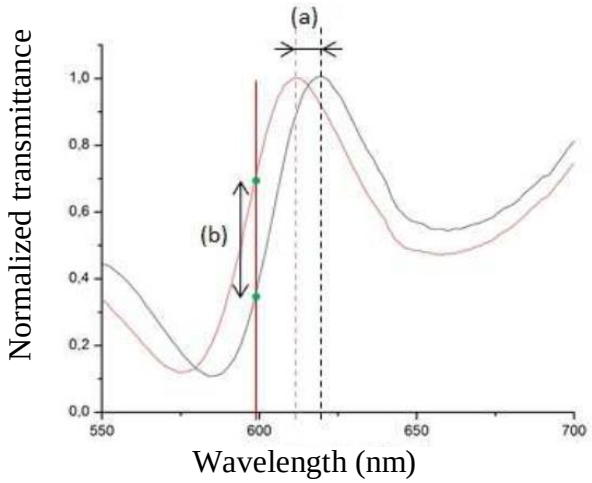

Figure II.20 Methods of monitoring a change in refractive index (a) monitoring transmission peak, (b) variation in intensity transmitted at fixed wavelength.

II.3 Sensitivity and figure of merit:

The intrinsic sensitivity introduced in defines how the plasmon oscillation (characterized by β) intrinsically changes with the dielectric environment (n). This sensitivity is independent of the excitation or the modulation of the surface plasmons. To fully quantify the overall sensitivity, an external sensitivity needs to be included:

$$S_{RI} = \frac{\partial P}{\partial Re\{\beta\}} \frac{\partial Re\{\beta\}}{\partial n} \qquad \textbf{Eq.II. 86}$$

Where P is the sensor's optical output, and the external sensitivity $S^{ext} = \partial P/\partial Re\{\beta\}$ defines the sensitivity of the optical output to the variation of the surface plasmon oscillation. This external sensitivity mainly depends on the methods of excitation and modulation.

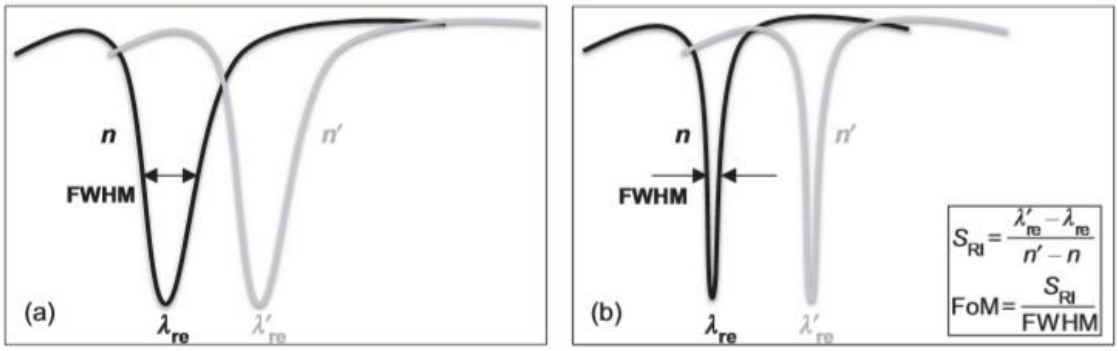

Figure II.21 The definitions of the sensitivity (SRI) and figure of merit (FoM). The sensor shown in (a) has the same sensitivity as, but a different FoM from, sensor (b).

The overall sensitivity SRI therefore represents the sensitivity of the optical output to the variations of the refractive index of the dielectric environment. For instance, the modulated optical output is the incident wavelength in resonance with the propagating SPP (i.e. λre). The overall sensitivity is then:

$$S_{RI} = \frac{\partial \lambda_{re}}{\partial n} = \frac{\partial \lambda_{re}}{\partial Re\{\beta\}} \frac{\partial Re\{\beta\}}{\partial n} = S^{ext} S^{int} \qquad \textbf{Eq.II. 87}$$

In an SPR sensing experiment, however, it is impractical to directly measure the refractive-index change (i.e. ∂n). Instead the sensitivity to the change in measurand (e.g. the analyte concentration *c*) is more commonly employed, for example,

$$S_{RI} = \frac{\partial \lambda_{re}}{\partial c} = \frac{\partial \lambda_{re}}{\partial n} \frac{\partial n}{\partial c} = S_{RI} E \qquad \textbf{Eq.II. 88}$$

Where the additional term *E* accounts for the binding efficiency, i.e. how efficiently the presence of analyte at concentration *c* is converted into a change in the refractive index *n*. From the design perspective, S_{RI} and *E* can be dealt with independently. In order to design a highly sensitive SPR sensor structure, the focus should be on optimizing S_{RI}. On the other hand, the binding efficiency *E* is more relevant when one needs to design a good element to bind the target analyte efficiently. In addition to the sensitivity, the other term employed to evaluate the performance of a surface plasmon biosensor is the figure of merit (FoM). The FoM is expressed in terms of both the sensitivity and the line width of the resonance peak (i.e. the full width at half maximum (FWHM)),

$$FoM = \frac{S_{RI}}{FWHM} \qquad \textbf{Eq.II. 89}$$

In general, the sharper the resonances peak, the higher the FoM. Essentially, the target in designing an SPR sensor is to increase both the sensitivity and the FoM.

There is two more significant sensor attributes that are:

-Resolution:

The resolution of a sensor is the smallest change in refractive index that can be measured by the entire measurement system. It therefore gives an idea of the possible detection limit, it depends a lot on the measurement system, the performance of each component (light source, detectors, quality of the coupler, etc.). In particular, the notion of noise is very important here, the noise level will be a determining factor for good resolution. Finally, note that each different system will have a different resolution, even if they rely on the same interrogation mode for tracking the refractive index.

-Dynamic range:

Dynamic range is the range of refractive index values that can be effectively measured with our system. It depends both on the coupler, and also on the associated measuring systems. There is also a trade-off between dynamic range and resolution.

II.4 MIM temperature sensor:

The basic fundamentals for a MIM structure are detailed in the first chapter.

Characterized by the following specific relation:

-The dispersion relation for TM mode in a MIM structure which has been previously defined in

-And the Drude formula for the complex relative permittivity of the used metal.

Furthermore temperature sensor can be realized by manipulating the electromagnetic properties of the SPP, utilizing the change in the refractive index of the temperature sensing material caused by the ambient temperature. In this work, we chose “thermo-optic liquid” ethanol as our sensing material because of its high temperature coefficient of refractive index. Ethanol is a preferable choice for low temperature sensing with a melting point of −144.3 °C and a boiling point of 78 °C. Generally, the relation between the refractive index of liquid sensing material and ambient temperature can be depicted by the following equation [24]:

$$n = n_{liq} + \frac{dn}{dT}(T - T_0) \qquad \textbf{Eq.II. 90}$$

Where dn/dT is the temperature coefficient of refractive index of the liquid sensing material which indicates the sensitivity of the liquid to temperature change, n_{liq} represents the refractive index at the reference temperature T_0 and T is the ambient temperature. Therefore, it is easy to obtain the relation between the refractive index of ethanol and temperature and the formula is given by:

$$n = 1.36048 - 3.94 \times 10^{-4}(T - T_0) \qquad \textbf{Eq.II. 91}$$

Where T_0 is 20 °C, which is the room temperature. Eq.II. 91 represents a linear relation between refractive index n of ethanol and ambient temperature. Comparing to the temperature coefficient of ethanol, the influences of temperature on the substrate and silver are negligible.

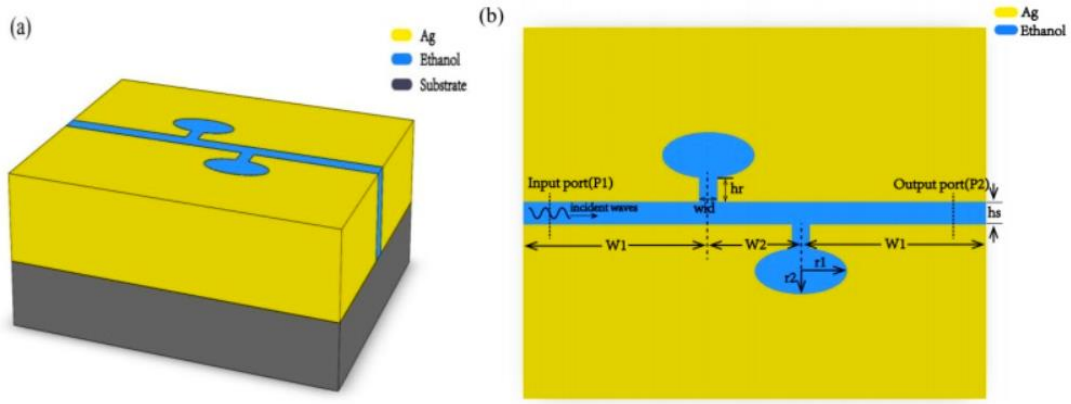

Figure II.22 An example schematic diagram of the temperature sensor based on metal-insulator-metal waveguides is shown. (a) Schematic diagram of the three-dimensional structure. The two layered structure is clearly displayed in the picture, composed of a waveguide layer and a quartz substrate layer. (b) The top view of the MIM waveguide layer. The ethanol-sealed cavities (blue in the picture), composed of two ellipse resonators, two rectangular tubes and a straight waveguide, were sandwiched by two silver layers.

II.5 Thermal properties of metallic nanoparticles:

II.5.1 Thermal conductivity of heterogeneous media:

Consider a nanostructure attached to a substrate of thermal conductivity κ2 in a homogeneous medium of thermal conductivity κ1. This is the practical case of nanostructures made by electronic lithography deposited on a substrate. To rigorously solve this configuration, we must consider the heat conduction equation in the two media considered by separating the contributions of the nanostructure in contact with the two media. There is another much simpler method which gives a satisfactory approximate result which is inspired by electrostatics.

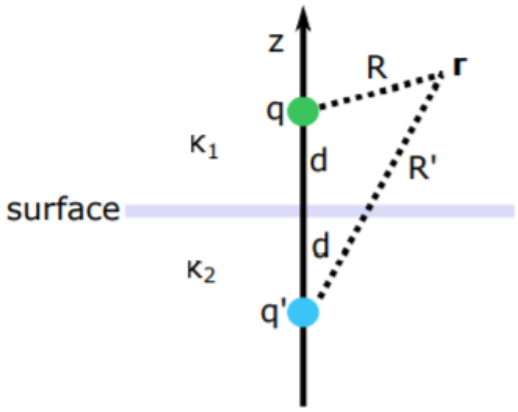

Figure II.23 Diagram of the method of images derived from electrostatics**.**

The presence of a planar interface separating the two media makes it possible to compare this case with the potential distribution created by a charge with an interface between two dielectric media. The temperature rise ΔT can be written as follows:

$$\Delta T = QG(\boldsymbol{r}, \boldsymbol{r}') \qquad \textbf{Eq.II. 92}$$

Where Q represents the power absorbed by the nanostructure and G(r,r ′) designates a thermal Green function. By analogy with the method of images derived from electrostatics, the thermal Green function takes the form [53] :

$$G(\boldsymbol{r}, \boldsymbol{r}') = \frac{1}{4\pi k_2}\left[\frac{1}{R} + \left(\frac{k_2 - k_1}{k_2 + k_1}\right) 1/R'\right] \quad z \geq 0 \qquad \textbf{Eq.II. 93}$$

$$G(\boldsymbol{r}, \boldsymbol{r}') = \frac{1}{4\pi k_2}\frac{1}{R}\left(\frac{2k_2}{k_2 + k_1}\right) \quad z \leq 0$$

Where

$$R = \sqrt{(x - x')^2 + (y - y')^2 + (z - d)^2} \qquad \textbf{Eq.II. 94}$$

$$R' = \sqrt{(x - x')^2 + (y - y')^2 + (z + d)^2}$$

With *d* the distance between the center of the nanostructure and the interface and the position vectors **r**(x, y, z) et **r′**(x′ , y′ , z′) in Cartesian coordinates. For two interfaces, this thermal Green function becomes more complex (additional information from [54]).

Regarding the temperature rise within the nanostructure, the expression gives for z = 0:

$$\Delta T_{NP} = Q \frac{1}{4\pi} \frac{1}{R} \left(\frac{2}{k_2 + k_1}\right) \qquad \textbf{Eq.II. 95}$$

That corresponds to the temperature rise of the nanostructure if it was immersed in a medium of thermal conductivity$\frac{2}{k_2+k_1}$.

In this model of thermal conductivity of heterogeneous media, we did not take into account the influence of a real interface on a heat flow transmitted between two media separated by it. A temperature discontinuity, associated with an interface thermal resistance, is generally observable at an interface separating two distinct material media.

Nanostructure under static heating:

In static conditions, the temperature rise inside the nanoparticle is written:

$$\Delta T_{NP}^{0} = \frac{Q_0}{C_{th}} \qquad \textbf{Eq.II. 96}$$

Where Q_0 is the power absorbed by the nanoparticle and C_{th} its thermal capacity. For the temperature rise outside the nanoparticle, the expression becomes:

$$\Delta T^{0}(r) = \frac{Q_0}{C_{th}} \frac{R}{r} \qquad \textbf{Eq.II. 97}$$

The average temperature inside the nanoparticle over a period of modulation $T = 1/2\pi\Omega$ is $\Delta\overline{T_{NP}}(t) = \Delta T_{NP}^{0}$. When we manage to measure experimentally the temperature rise of a nanoparticle under modulated heating, the result is that it is uniform and strictly equal to the case static.

For nanostructures lithographed on a substrate, the thermal capacity C_{th} differs from nanoparticles immersed in a homogeneous medium due to the heterogeneity of the environment of the nanostructure. Its thermal conductivity can indeed be approximated by [55]

$$k_m = \frac{k_{sub} + k_{sup}}{2}$$

For a nanostructure deposited on a substrate of thermal conductivity κ_{sub} and immersed in a superstrate of thermal conductivity κ_{sup}. The thermal conductivity of a medium depends on, furthermore, of its temperature $\kappa_m(T)$ but the temperature scales involved in nanoplasmonics radically minimize this variation with temperature if although $\kappa_m(T) \simeq \kappa_m$. The power absorbed by the Q_0 nanostructure also depends on the temperature of the nanostructure through its permittivity electric ϵ (T) varying with temperature.

The thermal dependence of the dielectric permittivity ϵ (T) also suggests a dependence of the plasmon resonance of metallic nanoparticles with temperature.

II.5.2 Dependence of plasmon resonance on temperature:

The properties of localized plasmon resonance of a volume V nanoparticle depend on its temperature. For gold nanoparticles, we observe a redshift and widening of the plasmon resonance with the temperature. Two main mechanisms have been associated with this modification of resonance:

- Electron-phonon scattering within the nanoparticle;

- Thermal expansion of the volume of the nanoparticle.

The respective contribution of these two phenomena has been highlighted in [56].

The population of phonons within the particle increases with temperature according to the Debye model inducing an increasing electron-phonon collision rate. This electron-phonon collision rate is found in the expression of the relaxation constant γ (T) of the LSPR:

$$\gamma(T) = \gamma_{\infty}(T) + A\frac{v_F}{R} \qquad \textbf{Eq.II. 98}$$

where $\gamma\infty$ (T) represents the size independent relaxation constant due to the scattering of free electrons, v_F the Fermi speed in the metal, R the radius of the nanoparticle and A a theoretical constant. The temperature dependence of $\gamma\infty$ (T), specified in [56], contributes to both the enlargement and the shift towards the red of the resonance. By comparison with experimental results, it has been shown that electron-phonon scattering plays a key role in the enlargement of the plasmon resonance. Furthermore, thermal expansion of the nanoparticle, depending on the interatomic potential of the nanoparticle, mainly contributes to the redshift of the resonance. For 20 nm gold nanoparticles undergoing a temperature rise of 200°C, the plasmon resonance shifts ~ 12 nm in the red and its broadening corresponds to ~ 5% of its initial width. Given the temperatures involved

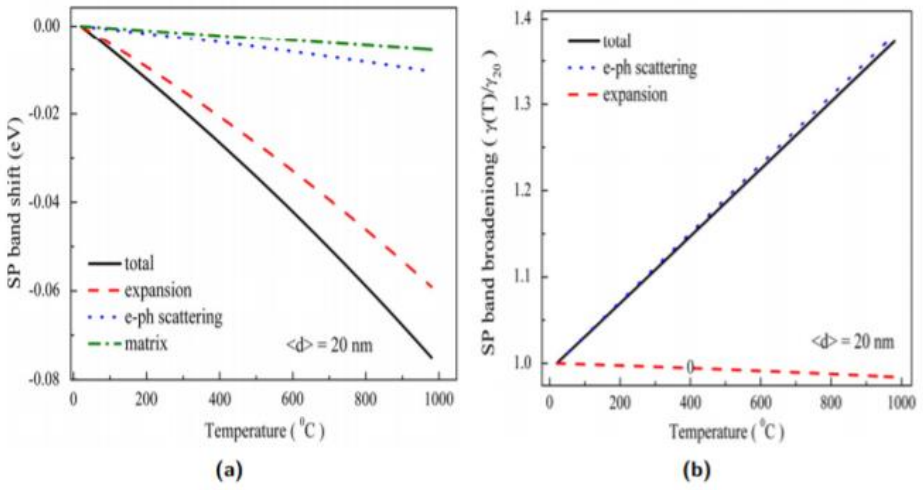

Figure II.24 Calculations of the contributions of the different thermal mechanisms influencing the LSP. (a) Spectral shift and (b) spectral broadening of the LSP of a 20 nm diameter spherical gold nanoparticle in a silica matrix. The thermal expansion of the volume, in mid-long dotted lines the thermal dependence of the dielectric permittivity of silica, in short dotted lines the electron-phonon scattering of the nanoparticle. [56]

II.6 Modulation methods:

In general, there are five different plasmonic characteristics to modulate: the resonance angle, resonance wavelength, intensity, phase, and polarization [30]. For angular modulation, the coupling strength is measured at a fixed incident wavelength and multiple angles of incidence, and the angle of incidence yielding the strongest coupling (i.e. the resonance angle) is determined. This is often used in prism-coupling SPP-based sensors. For wavelength modulation, the coupling strength is measured at a fixed angle of incidence and multiple incident wavelengths, and the incident wavelength yielding the strongest coupling (i.e. the resonance wavelength) is

determined. Wavelength modulation is the most widely used modulation method, and is often seen in SPP-, LSPR-, EOT-, and Fano-resonance-based plasmonic sensors.

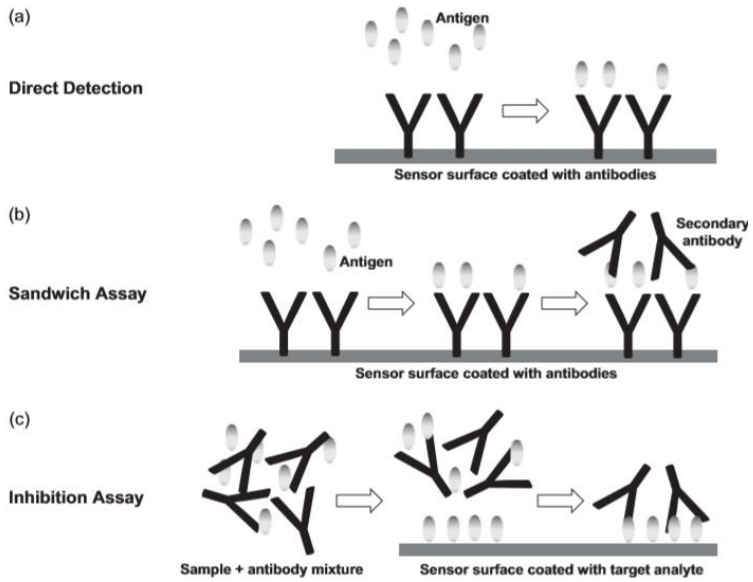

Figure II.25 The three different assay formats: direct detection, sandwich assay, and inhibition assay.

II.7 Design methods:

Among the three components of a plasmonic sensing system, this chapter will mainly focus on the design and optimization of the sensor's structure, in order to achieve the highest possible sensitivity and FoM. In this section, two design methods will be introduced. The first one is an analytical model known as the "*N*-layer model," in which one calculates the reflection and transmission of light through *N*-layers of materials. It is often used to design a prism-coupled SPP-based plasmonic sensor. When the sensor's structure becomes more complicated, involving nanostructures, such as grating, slits, and holes, a more comprehensive model based on the finite-element method (FEM) is required.

II.7.1 The *N*-layer model:

We consider the situation when light is reflected from an N-layer composite structure, which consists of layer 1, 2,..., N −1, N as shown in Fig. 7.9. The thickness of each layer is d_k, where the integer k =2, 3, 4,..., N −1 denotes the layer number. The first and last layers are assumed to be infinitely thick. The reflection coefficient r (and hence the reflectance R =| r|²) is expressed as [27]:

$$r = \frac{(M_{11} + M_{12}q_N)q_1 - (M_{21} + M_{22}q_N)}{(M_{11} + M_{12}q_N)q_1 + (M_{21} + M_{22}q_N)} \quad \textbf{Eq.II. 99}$$

Where the four matrix elements M_{ij} (i, j =1,2) are defined as

$$M_{ij} = \sum_{k=2}^{N-1} Mk,\ i,i = 1,2. \quad \textbf{Eq.II. 100}$$

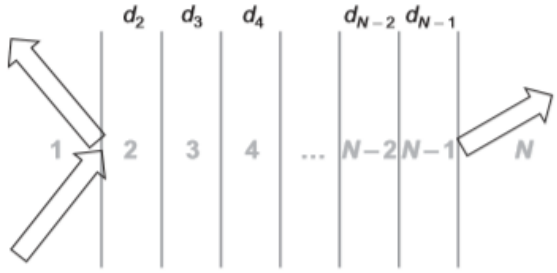

Figure II.26 The N-layer model for SPR measurement.

Here, M_k is a 2×2 matrix related to the *k*th (*k* runs from 2 to N −1) layer's optical property and thickness:

$$M_{ij} = \begin{bmatrix} \cos\beta_k & -iq_k \sin\beta_k / q_k \\ -iq_k \sin\beta_k & \cos\beta_k \end{bmatrix} \quad \textbf{Eq.II. 101}$$

Where

$$\beta_{ik} = d_k \frac{2\pi}{\lambda_0}(\varepsilon_k - n_1^2 \sin^2\theta_1)^{1/2} \quad \textbf{Eq.II. 102}$$

And
$$q_k = \begin{cases} \left(\frac{\mu_k}{\varepsilon_k}\right)^{1/2} \frac{(\varepsilon_k - n_1^2 \sin^2\theta_1)^{1/2}}{\varepsilon_k^{1/2}} & for\ a\ TM\ wave, \\ \left(\frac{\varepsilon_k}{\mu_k}\right)^{1/2} \frac{(\varepsilon_k - n_1^2 \sin^2\theta_1)^{1/2}}{\varepsilon_k^{1/2}} & for\ a\ TE\ wave. \end{cases} \quad \textbf{Eq.II. 103}$$

Here, d_k is the *k*th layer's thickness, λ_0 is the vacuum wavelength of the incident light, θ_1 is the angle of incidence in the first layer with refractive index n_1, and ε_k denotes the *k*th layer's

dielectric permittivity. Through a series of numerical calculations using the above equations, the reflectance from a multilayer structure could be obtained.

II.7.2 The FEM model:

The handy *N*-layer model is useful for layered sensing structures. For complicated sensing structures involving nanostructures, FEM simulation is needed. Figure II.27 shows a schematic representation of the FEM model. The model solves Maxwell's equations and calculates the light–matter interactions of any geometry. The model takes two inputs, which are the material property (most commonly the refractive index *n* or the dielectric permittivity ε, where ε=n2), and the exact size of each part of the structure. The whole structure is drawn and divided into small grids. Maxwell's equations are solved for each grid, with the continuity condition being maintained from grid to grid. Simultaneously, a certain boundary condition at all outer boundaries need to be satisfied as well. Once there is a convergent solution, we are able to know the distributions of the electric field ***E***, magnetic field ***H***, electric flux density ***D***, and magnetic flux density ***B*** in the structure. Then post-processing is done to extract the needed information, for example, the optical power-absorption spectrum, the near-field distributions, and so on.

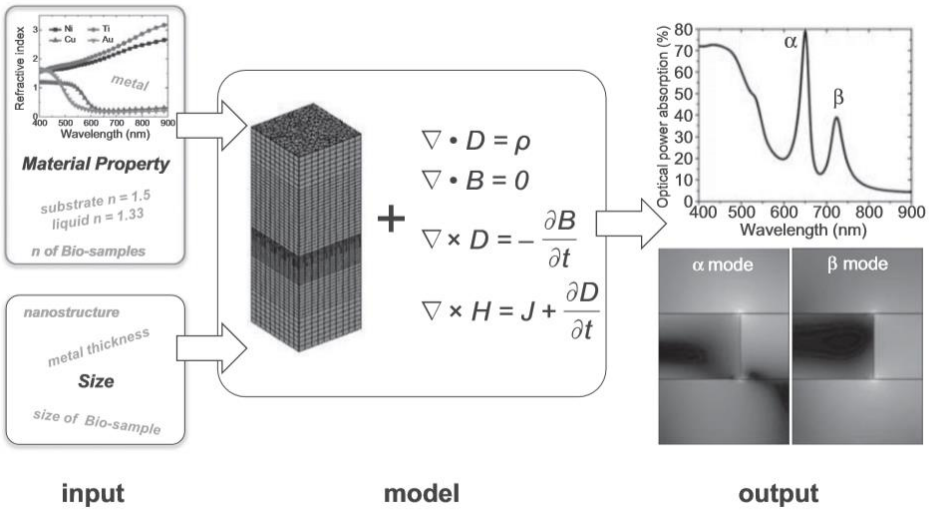

Figure II.27 A schematic representation of FEM simulation showing the input, the output, and the calculation model.

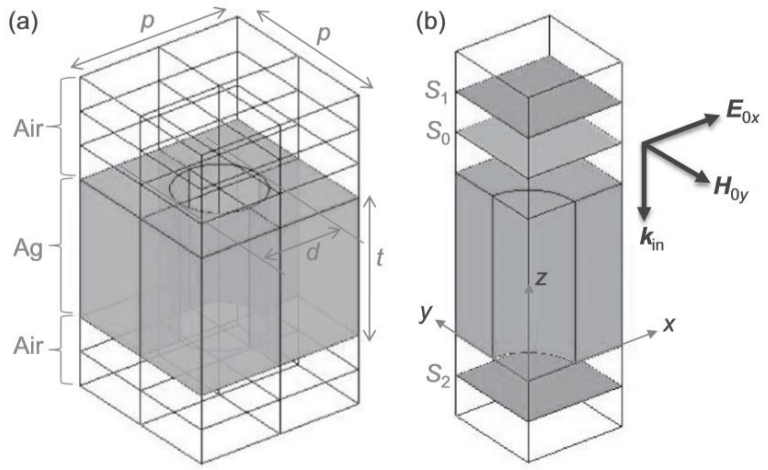

Figure II.28 (a) The unit cell for simulating light propagating through a two-dimensional cylindrical hole array (repeating in the *x* and *y* directions) in a suspended Ag film in air, i.e. air/silver/air, where *p*, *d*, and *t* are the pitch of the array, the diameter of the hole, and the thickness of the Ag film, respectively. (b) A quarter of the unit cell, where S_0 is the surface used to set up the incident light wave, and the surfaces S_1 and S_2 are used to calculate the reflected and transmitted power, respectively. For simplicity, a linearly polarized plane wave traveling in the−*z* direction with the electric field polarized in the *x* direction is assumed. Adapted from [60].

Here we will use a nanohole array structure as an example to demonstrate the application of the FEM model [60]. When light illuminates a nanohole array milled in a metallic film, some of the incident optical power is reflected, some is absorbed, and the rest is transmitted. To understand how the plasmonic resonance is generated at the surface of a patterned metal film, we study the nanohole array in a silver film suspended in air. Figure II.28 (a) depicts a unit cell of the nanohole array structure, where the pitch of the hole array is p, the diameter (and the depth) of each hole is d (and t). Owing to the geometrical symmetry, only a quarter of the unit cell needs to be simulated, as shown in Fig. 7.11(b).

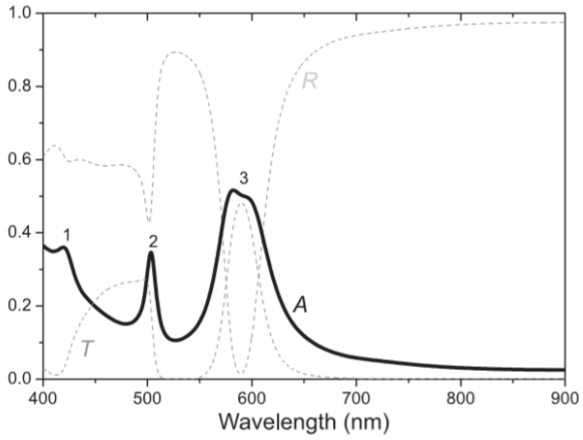

Figure II.29 Simulated spectra of absorptance A, reflectance R, and transmittance T for a cylindrical hole array (p =500nm, d =250nm) fabricated in a 400-nm-thick free-standing Ag film. Adapted from [60].

In the simulation, the three-dimensional Maxwell equations are solved using the FEM. The material property of silver ε_{silver} (λ_0) is taken from Palik's handbook [61]. A normally incident plane-wave source (λ_0 =400–900nm) is set up at the surface S_0. For simplicity, a linearly polarized plane wave traveling in the $-z$ direction with the electric field polarized in the x direction is assumed. As the incident wave strikes the structure, it will be absorbed, reflected, and transmitted. The absorbed power P_{abs} is computed through the volume integration of the resistive heating (i.e.$\int_V \mathbf{J}\cdot\mathbf{E}\, dV$) in the silver film, with **J** the current density and **E** the electric field. The reflected power P_{ref} and the transmitted power P_{tra} are calculated through the surface integration of the power flow (i.e.$\oint S(E \times H)\cdot n\, dS$) over the surfaces S_1 and S_2, respectively. Here $\boldsymbol{E} \times \boldsymbol{H}$ represents the Poynting vector, and n is the unit normal to the surface S. The absorptance A, reflectance R, and transmittance T are the ratios of the absorbed power, the reflected power, and the transmitted power to the incident power, respectively. The simulated spectra of absorptance, reflectance, and transmittance are plotted in Figure II.29, where the pitch of the hole array is 500 nm and the diameter (the depth) of each hole is 250 nm (400 nm). The absorptance spectrum of the nanohole array (A) exhibits three resonance peaks: peak 1 at 420nm, peak 2 at 504nm, and peak 3 at 582nm.

To explore the physics behind this, the total electric field $|\boldsymbol{E}| = \left(E_x^2 + E_y^2 + E_z^2\right)^{1/2}$ distributions (Vm^{-1}) in the x–y planes and in the z–x plane are shown in Fig. 7.13. The two x–y planes are cut at the front (z = t) and back (z = 0) silver/air interfaces, respectively, whereas the z–x plane is cut through the center of the nanohole (y = 0). From the plot, strong electric fields are observed

around the rim of the nanohole for two absorption peaks: peaks 1 and 3, which show a distinct feature of the SPR. However, peak 2 does not show similar characteristics, which suggests that some other mechanism such as one involving the waveguide modes is responsible.

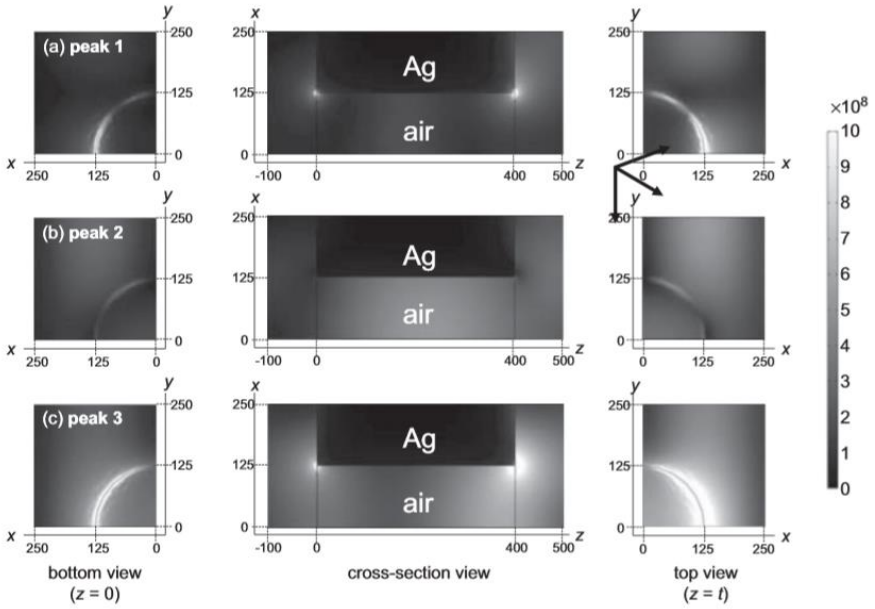

Figure II.30 The electric-field distribution (Vm^{-1}) from the bottom view (*x*–*y* plane, z = 0), the cross-section view (*z*–*x* plane, y = 0), and the top view (*x*–*y* plane, z = t), at three wavelengths: (a) 420 nm, (b) 504 nm, and (c) 582 nm, which correspond to the absorptance peaks 1, 2 and 3 shown in **Figure II.29**(b). Adapted from [60].

In the example (air/silver/air structure) presented above, we have demonstrated that the absorptance *A*, reflectance *R*, and transmittance *T* can be calculated, and the electromagnetic field distributions can also be plotted to show vividly what the plasmonic modes look like. In most sensing experiments, it is more convenient to measure the reflectance *R*. The resonant excitation of the surface plasmons is commonly observed as a dip in the reflectance at a specific wavelength. The dip in fact results from the absorption of optical energy in the metal, but the optical power absorption is difficult to measure. On the other hand, our FEM model can directly calculate the optical energy absorption, which does show a peak at the same resonance wavelengths. Therefore we can use either the reflectance *R* or the absorptance *A*, or even the transmittance *T*, to find the resonance wavelengths in our FEM model.

The surface plasmons are extremely sensitive to changes in the refractive index near the metal surface within the range of the surface plasmon field. Such a change may result in a shift in the resonance wavelength of the incident light or a change in the intensity of the reflected light. To

theoretically predict the sensitivity to the refractive-index change, we will need to run a pair of simulations (with two different dielectric environment) to see this shift. Then the sensitivity is calculated by dividing the shift of the resonance wavelength by the refractive-index change, with the answer in units of nm per RIU.

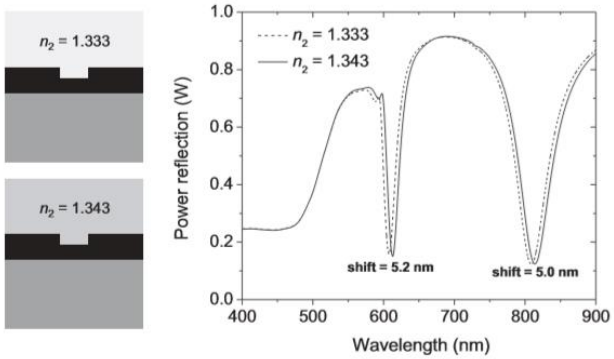

Figure II.31 An example to show how to evaluate the sensitivity. Two independent simulations are performed with two different refractive indexes, 1.333 and 1.343. For the change in refractive index change of 0.01, the resonance wavelength shift defines the sensitivity of a plasmon mode.

Figure II.31 shows an example of how the sensitivity can be evaluated, where simulations with n_2=1.333 and n_2=1.343 are performed separately. We plot their power reflection spectra on a single figure and can easily see the difference between the two calculations. From Figure II.31, we observe two surface plasmon modes in each simulation. The first mode around a resonance wavelength of 600 nm will shift by 5.2 nm and the second mode around 800 nm will shift by 5.0 nm. This corresponds to a sensitivity of around 500–520 nm per RIU. By applying the same approach, we are able to model and evaluate the sensitivity of any proposed sensing structure.

I.8 Conclusion:

In conclusion we have presented within this chapter some basic information regarding SP sensors their characterization and their conception along with different modeling and design methods and the strong ability to confine energy of surface plasmon polaritons beyond the diffraction limit renders MIM structure more attractive for our proposed application, and the high sensitivity to minute changes in the temperature makes the plasmonic sensor suitable for applications where conventional sensors can’t be applied.

Chapter III: Results and interpretations

III.1. Introduction:

In this chapter, we propose a plasmonic structure to construct a temperature sensor based on a metal–insulator–metal (MIM) waveguide (using the plasmon surface resonance "SPR") coupled with a cavity then a defect.

The proposed work aims at developing a Metal-insulator-metal (MIM) plasmonic waveguide that provides a high light confinement that is suitable for the sensing application. Sensor is created and simulated using an RSoft tool which is based on finite difference time domain; which is a numerical tool used to solve the Maxwell's equation. We investigated the performance of vertical metal-insulator-metal (MIM) structures as plasmonic temperature sensors, the numerical simulation results show that the resonance dips of the structure have a high resonant transmission contrast ratio and that the resonance wavelengths have a near-linear relationship with the refractive index of the dielectric material in the cavity.

The numerical simulation results obtained from the transmission spectra are used to analyze the sensing characteristic of the structure. We will first study 'the subwavelength' and the refractive index of the proposed structure, as well as the geometric parameters of the cavity and the defect. In the second step we will try to improve the sensitivity of our structure.

III.2 Representation of R-SOFT CAD

III.2.1 Modeling Methods

The electromagnetic modelling of the plasmonic guides properties is generally requires a large investment in programming and numerical analysis. The main computational techniques used for plasmons are transfer matrix methods, lattice diffraction theories, and finite difference time domain (FDTD). The calculation of finite structures is based on a Perfectly Matched Layer (PML) method.

III.2.2 Rsoft CAD Environment

RSoft CAD is basic software for the photonics and the plasmonics studies. It allows researchers and engineers to create a design for different devices such as: waveguides, resonant cavities, and other plasmonic devices. In Rsoft, there are several integrated modules, each module performs a

specific function, among these modules are : BeamPROP, FullWAVE, BandSOLVE, GratingMOD and DiffractMOD (It acts as a management program for the passive simulation modules of the RSoft device).

III.2.3 The "FULL WAVE" Simulator

The numerical simulations were carried out with the Fullwave software. The Fullwave is an electromagnetic simulation software, based on the finite difference method in the time domain. The FDTD method is based on solving Maxwell's equations in a spatially and temporally discrete domain. This numerical allow developers to follow the evolution of the EM field over time at any point of the structure. We can thus obtain the maps of the EM field at any place and at any time. Knowledge of the evolution of the field as a function of time also allows information to be obtained on the spectral response of the structure.

This software can simulate structures (limited, infinite or periodic), formed by different materials which can be metallic or dielectric. Using Fullwave requires defining the materials that make up the structure with the help of electrical permittivity. It is also necessary to define the environment of the structure and therefore the boundary conditions. For this it is necessary to have absorbent conditions on the outskirts of the discretization domain (calculation) which makes it possible to avoid the parasitic reflections generated at the edges of the window of the FDTD calculation in order to simulate an open medium.

The objective of FullWAVE is to provide a set of simulations to calculate the propagation of light in waveguides of arbitrary geometries. The simulation is based on the FDTD (Finite Difference Time Domain) technique. FDTD is a method of directly solving Maxwell's equations in the time domain; it uses the numerical tool of finite differences. The responses can be obtained in the TE and TM fields simultaneously.

III.3 Waveguide Simulation Steps

III.3.1 CAD Program Window

The Rsoft CAD program window has a menu bar at the top of the window, a toolbar with several icons and the status line (see Figure III.32).

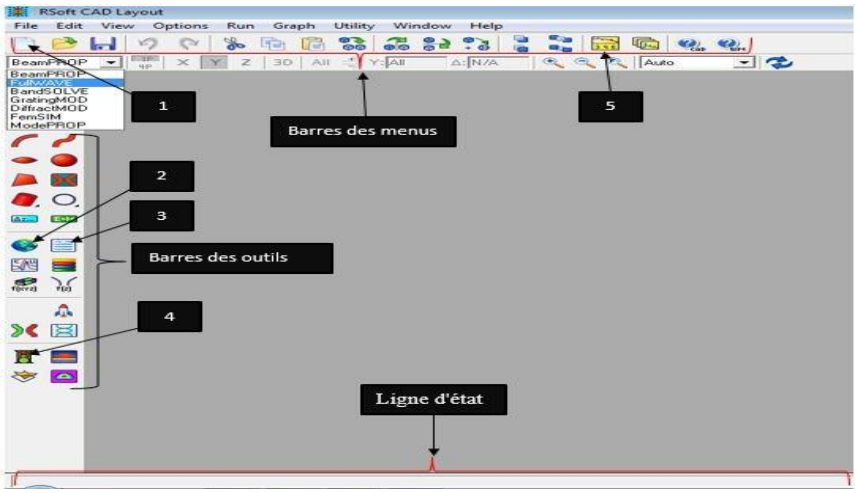

Figure III.32 The main window of the CAD program. of R Soft CAD, showing the menu bar above, the top and left toolbars, and the status line at the bottom.

III.3.a Create a New Circuit

To create a new circuit we will click on the icon (see number 1 in the Figure III.32) New circuit in the upper toolbar. Alternatively, we'll choose File / New from the menu. The start-up dialog in **Figure III.33** will appear.

You must fill in the index difference, which is the default index difference between the guiding layer and the substrate index (Background index), on the other hand, you must choose the simulation module among the six existing modules in the RSoft BandSOLVE, FullWave, BeamPROP / BPM or GratingMOD software. and choose the dimensions module (2D or 3D). After entering the information in the start window, we will click on OK to obtain the window shown in Figure III.34

III.3.b Generate The Structure

In this part we will show how to create a plasmonic structure in the CAD interface. Generally, there are several ways to create a structure in the CAD interface. However, the easiest way is to use one of the multiple layout utilities that are included with Full WAVE in the Toolbars (for **Figure III.33**).

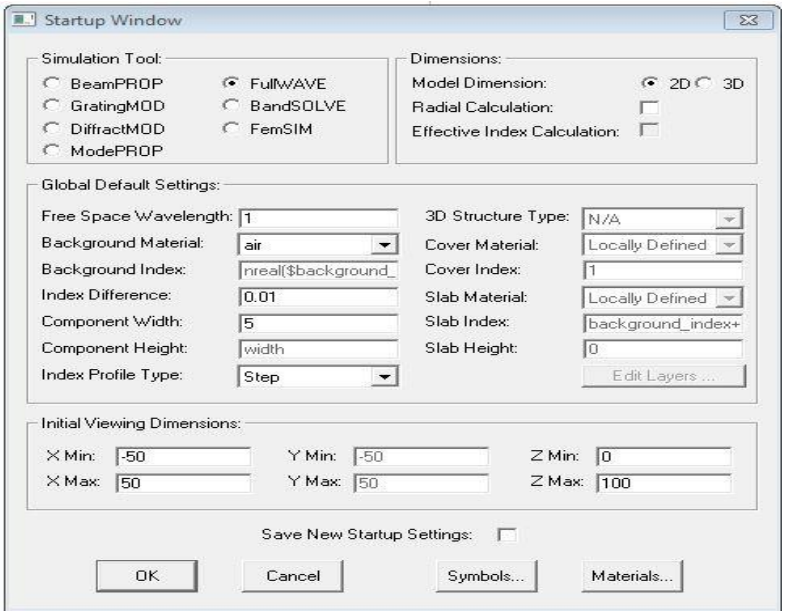

Figure III.33 The startup window: Parameters for creating row XZ.

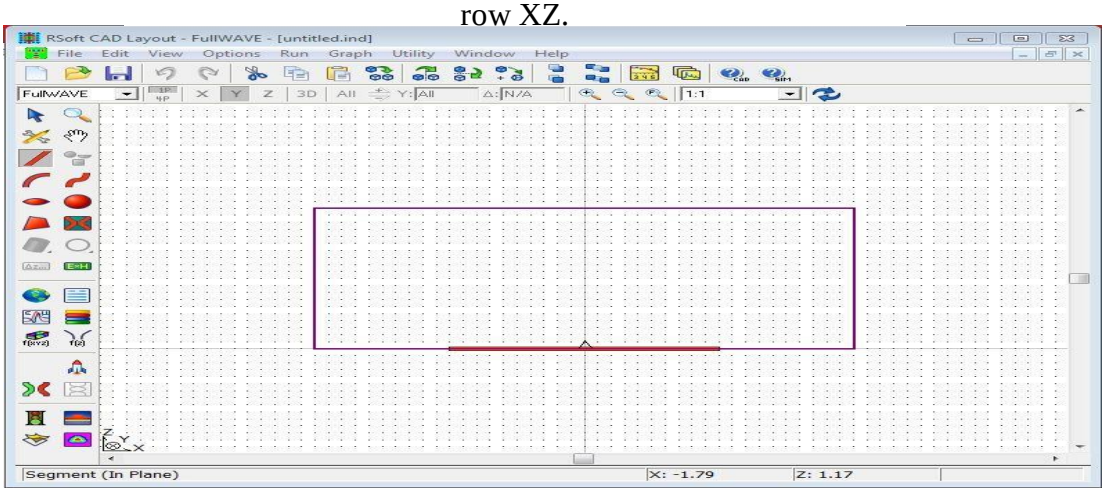

Figure III.34 New window to create a new component or new circuit.

Click on any shape in the toolbar and tap the middle of the program page. The figure appears on the page, Then click the right mouse button to display the information window. (Figure III.34)

After entering the various data (merge Priority, Material Properties, OX-OZ dimensions, etc.), click on the OK button to obtain the structure which appears on for example in Figure III.36

III.3.c Setting Global Parameters:

To set different properties of the structure such as the refractive index of a material, polarization and to choose simulation module Full WAVE from other modules that exist in RSoft we click on the icone (N2 in Figure III.32) (global setting). The below window appears (Figure III.37).

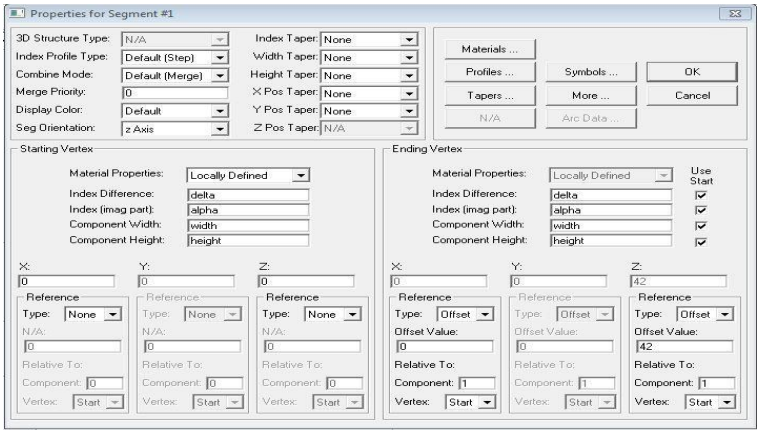

Figure III.35 New window to create a new component in the structure.

Creating a Waveguide:

We consider in this section a dielectric (air) waveguide of W1. To form the waveguide, the structure will be cut in two parts between these two parts there is the vacuum [air]. It is formed by removing some of the silver in the XZ direction, so the guide can be seen separated by a cavity plus a defect (see Figure III.36). To form a cavity, the structure will be cut in the middle just on the waveguide in two air guide parts 1 and 2 colored in blue with a similar dielectric "air" cavity between these two guides. In addition, the defect (red colour) of the central of this cavity will also be modified with the cavity of course to further optimize the resonance properties of this structure.

When the structure is well defined, the simulation must be carried out using the Full Wave simulation tool to calculate the transmission at the output of the guide. Before simulating, we must define the field by choosing the icon Edit Launch Field

Where the user can indicate the initial field for a simulation, then click on option to add the monitor at the end of the waveguide and click on the Perform Simulation icon where the user can indicate simulation parameters before performing it (see Figure III.37).

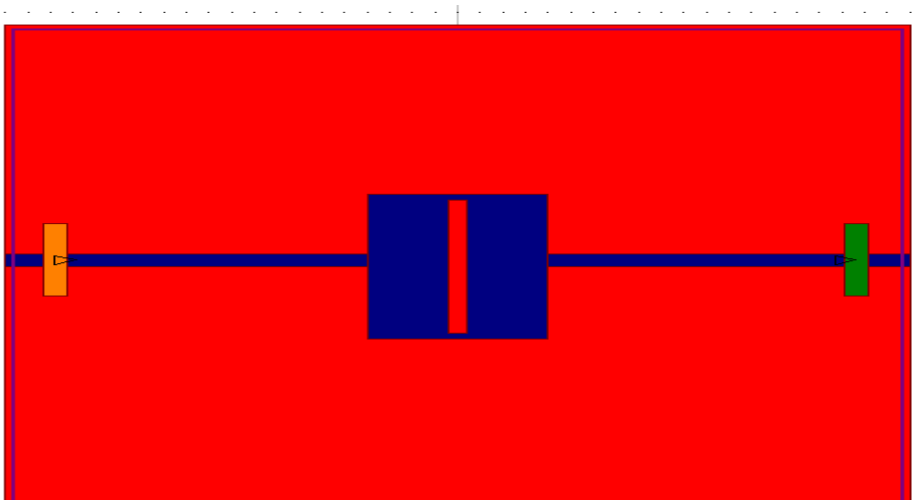

Figure III.36 The Rectangular Form of the Structure

III.3.d. Variables Definition:

Network customization: The global edit settings button lets you define network properties. In this example, we will create a square air cavity (n = 1) with a defect in the latter and the wavelength of the free space is 1.55µm (see **Figure III.42**).

Click on the icon (N3 for Figure III.32) (Edit symbols) in the CAD window, the table of symbols (Table editor) opens (**Figure III.38**). This array of symbols allows the user to both create or modify and integrate user-defined variables, these variables can be used to define almost any parameter of the structure (radius, period, l refraction index, number of ranges). These symbols correspond to the arrangements made in the New Circuit of the dialog box above. To define a new symbol, we click on new symbol then enter the name and the value of the symbol.

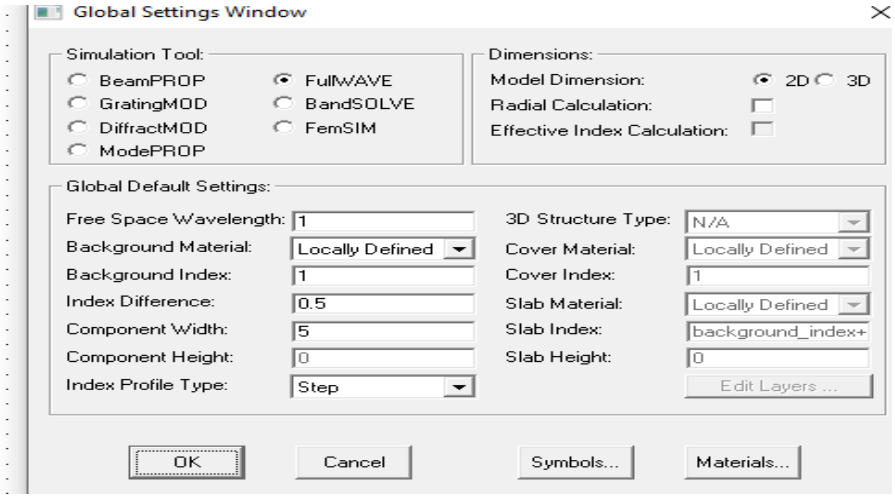

Figure III.37 Global Circuit Parameters Window: Global Arrangements

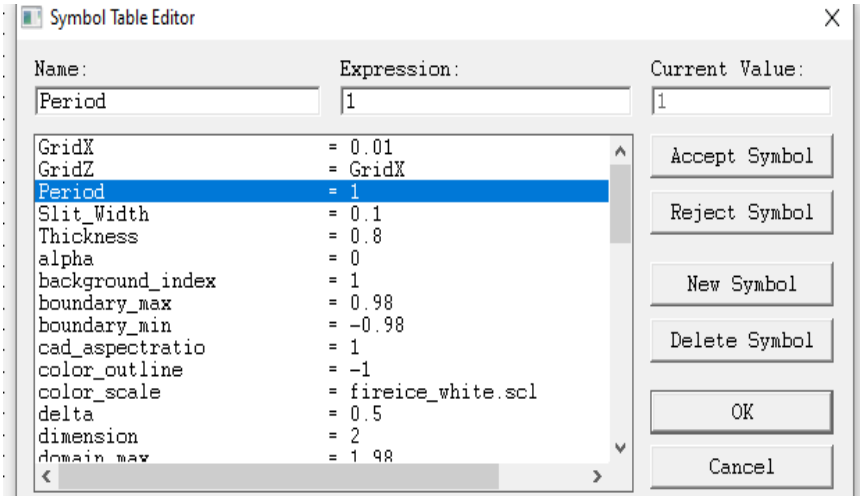

Figure III.38 The Symbol Table Editor.

III.3.e. Checking the Structure:

To verify our structure, we simulated the profile of the refractive index in the XZ plane (**Figure III.39** and **Figure III.40**).

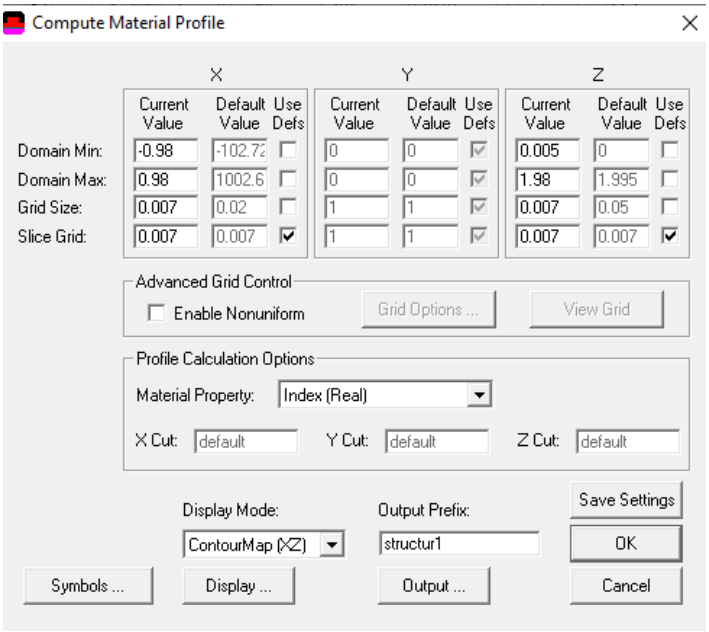

Figure III.39 Refractive index profile dialog box in the XZ plane

To create a straight guide of width port 2 in a direction ΓK orΓ M, all you have to do is place a rectangular shape in a different material in the direction specified. (see Figure III.41).

III.3.f Adjustment of Simulation Parameters:

To check the index distribution of the structure we have rectangular. The index profile button is pressed. To choose and adjust the simulation parameters, click on the Button (see number 4 in Figure III.32). Consequently, it appears the window corresponding to the simulation used (FullWave) As it is represented in Figure III.41.

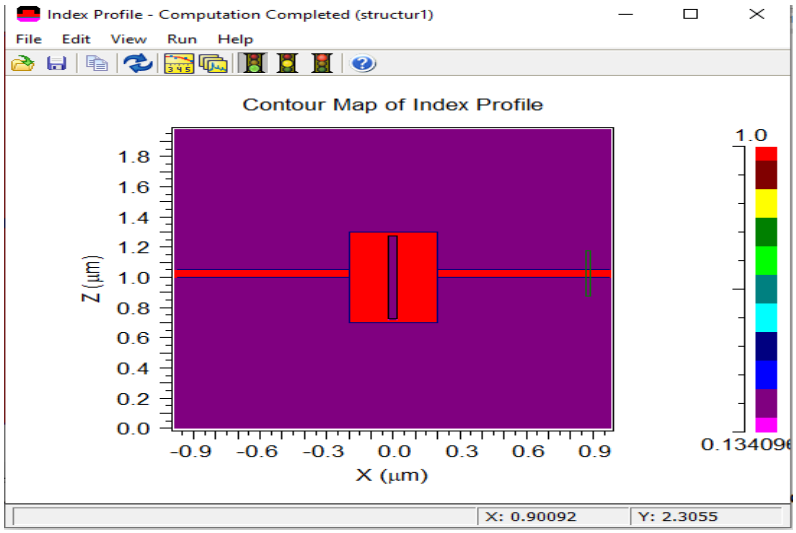

Figure III.40 Index profile Verification of the 2D plasmon structure:

We will choose Pulsed and $\Delta x = \Delta z = 0.007$ and number of iterations (Stop time) = 100 s. Once the numeric settings and other options are acceptable, click OK to start the simulation (start transmission).

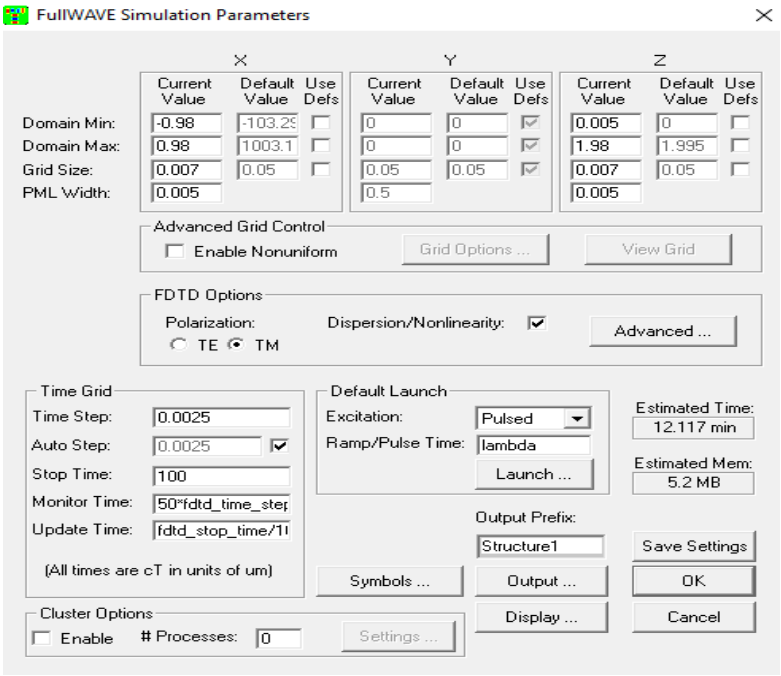

Figure III.41 Full WAVE simulation parameters window

III.3.g Reading the Results

In order to view or print the simulation results, we click on the icon (N5 for Figure III.32) of WinPLOT in the upper toolbar of the CAD window, and we choose the desired graph from the dialog that is present.

III.4. Modeling of the MIM Waveguide

A MIM waveguide structure is shown in **Figure III.42** The MIM plasmonic waveguide can propagate the SPP mode at the subwavelength scale with relatively low dissipation and a large distance of spread. Each of the metal-dielectric interfaces of the waveguide supports an SPP mode which propagates in the x direction. One would expect that when the space between the two interfaces is comparable to the decay lengths of SPPs in the dielectric, the modes of SPP will be coupled to each other [64]. Metal is silver and the dielectric in the core of the structure is assumed to be air with a refractive index n = 1.

The resonant wavelength of the design can be adjusted by varying the length and height of the cavity and the defect. For the simulation of the sensor operation, the FDTD method with as boundary condition, a perfectly matched absorbent layer is used. The characteristics of the filter are discussed in detail.

III.5 Structures and Simulation Method

Figure III.13 shows the structure of the designed plasmonic sensor which consists of a MIM waveguide laterally coupled to an I-shaped resonator. The sensor parameters w and d are respectively the width of the MIM waveguide, the height of the resonator. The frequency-dependent dielectric constant of silver is expressed by the Lorentz-Drude model:

$$\varepsilon(\omega) = \varepsilon_\infty - \frac{\omega_p^2}{\omega^2 + i\omega/\tau_0} - \frac{f_1\omega_p^2}{\omega^2 - \omega_0^2 + i\omega/\tau_b} \quad \text{(III.24)}$$

Where $\omega_p$is the plasmon frequency of the metal, tau_0Is $\sqrt{-1}$the relaxation time, ω is the frequency of interest, i denotes the complex number, and the contribution of the transitions

between bands at an infinite frequency (ie the static contribution) isε_∞. The new Lorentz term includes the Lorentz oscillator damping timeτ_b, the Lorentz resonance width$\omega_p$and a weighting factorf_1. The values of the various parameters for money are given in **Table III.2**.

Parameters	Values
ε_∞	3.7187
$\omega_p(rad/s)$	$1.396 * 10^{16}$
$\omega_0(rad/s)$	$6.496 * 10^{15}$
$\tau_0(s^{-1})$	$3.29 * 10^{-14}$
$\tau_b(s^{-1})$	$1.697 * 10^{-16}$
$f1$	0.4242

Table III.2 Various Parameters values of Silver (Ag)

The FDTD method implemented in the Fullwave module of Rsoft is used to study the transmission properties of this structure, with the absorbent boundary conditions of a perfectly matched layer (PML) in the x and z directions of the simulation domain. Light incident for the SPP mode excitation has TM polarization (the magnetic field is parallel to the y axis). In the numerical simulations and subsequent analyzes, the grid sizes in the x and z directions are taken as x=z=5nm and t=x/2c, which ensures numerical convergence in the method. The power source is placed at the Port 1 point and the reception is set at the Port 2 point to detect the transmitted power. Therefore, the power transmission factor is T=A. The method of auxiliary differential equations (ADE) is used to model dispersive materials in FDTD in the time domain, relating the polarization and the density of electric flux. In the calculations and the results which will follow, only the TM mode constitutes components E_x,$E_z$and H is taken into account because of its obvious excitation of the plasmon on metallic surfaces.

III.5.1 Presentation of The Studied Structure

III.5.1.a Proposed structure optimization:

The sensor using the waveguide is shown in **Figure III.42**. Its structure is composed a rectangle and a defect that can be filled with a material (liquid or gas).

First, we carried out a cavity guide coupling of a 2D structure and then a design of a sensor. In the simulation, Using the FDTD method, the transmission spectrum and electric field distribution of the optimized cavity (d1=600nm) with the refractive index of n (air) = 1, which is the resonance wavelength of the cavity. The light travels in the z direction. The structure is excited by the TM polarization. The steps of space in the x and z directions are ΔX and ΔZ. 2D structure, in what follows, we propose the design of a new plasmonic structure (MIM) in the case of Silver / air / silver. With d=550nm, W1= 50nm, L1=550nm, L2=40nm, d1=600nm. This parameters are fixed to this structure any change on d1 could cause a dispersion in the signal.

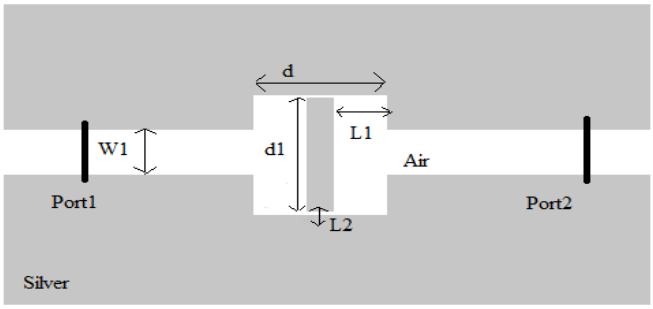

Figure III.42 Presentation of the studied structure.

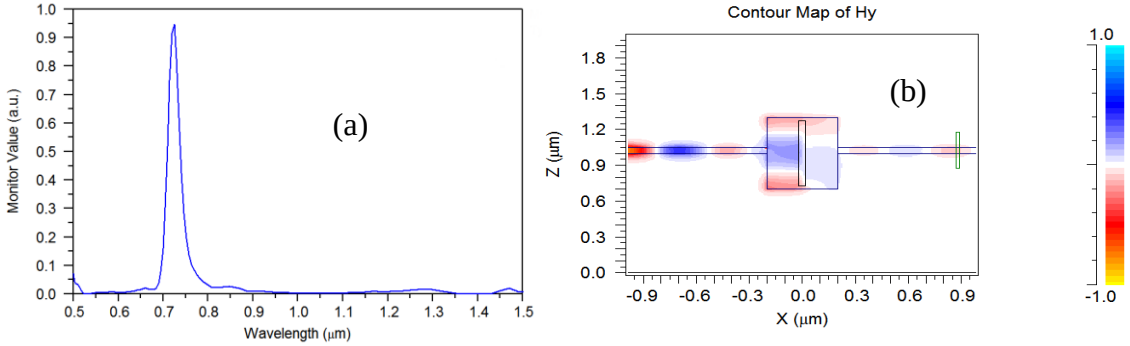

Figure III.43(a) Simulated transmission spectrum of the proposed sensing structure. **(b)** The contour profiles of the field distributions of |Hy| at wavelength of 722nm.

As can be seen, there is a narrow peak at the wavelength of = 722 nm, as shown in **Figure III.43**. Moreover, at the larger resonance wavelength, the change of the refractive index caused by the environment, temperature has a greater impact on the change of the resonance wavelength. As a result, the temperature sensitivity will be increased. Additionally, the sensitivity slightly increases with the coupling distance increasing at the same side length. Therefore, the temperature sensitivity of the plasmonic temperature sensor can be optimized not only by tuning the side length of the cavity but also the coupling distance.

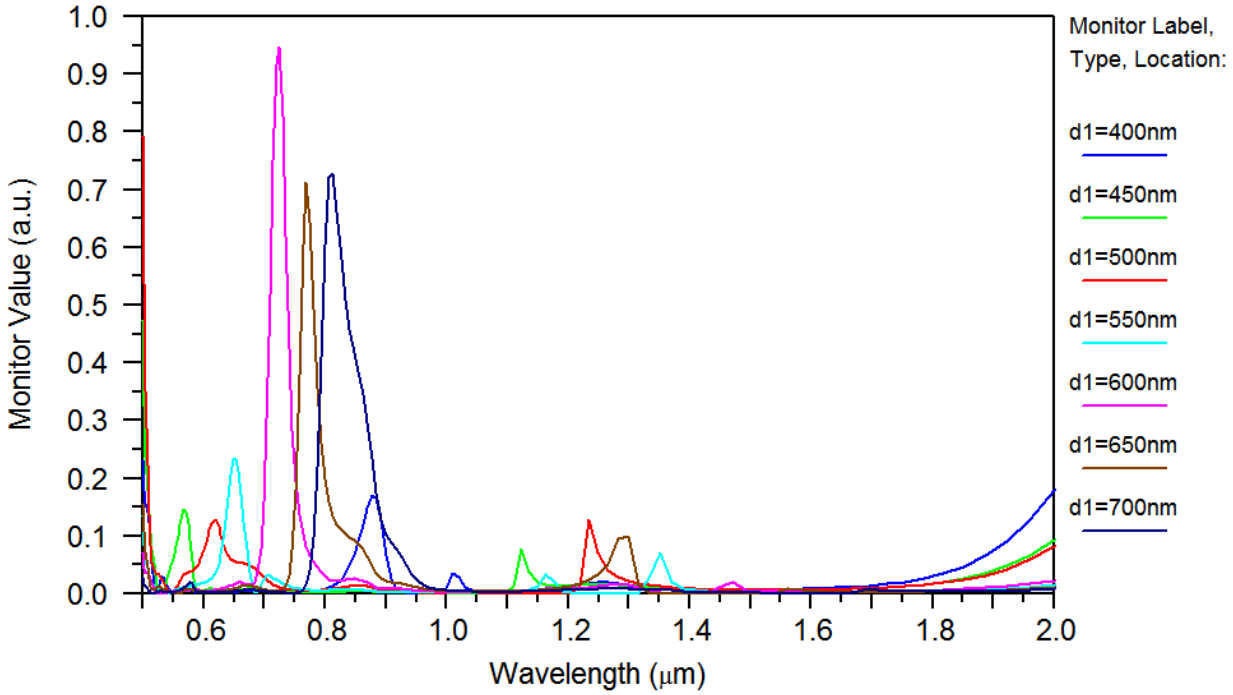

Figure III.44 transmission spectra of the MIM structure for different distances of"d1"

The transmission spectra in figure IV.2 obtained for different value of the distance d1, show that the transmission corresponding to the distance d = 600nm is the greatest compared to the other values of d1. The best transmission therefore corresponds to the distance d1 = 600 nm for the excitation wavelength of 722nm.

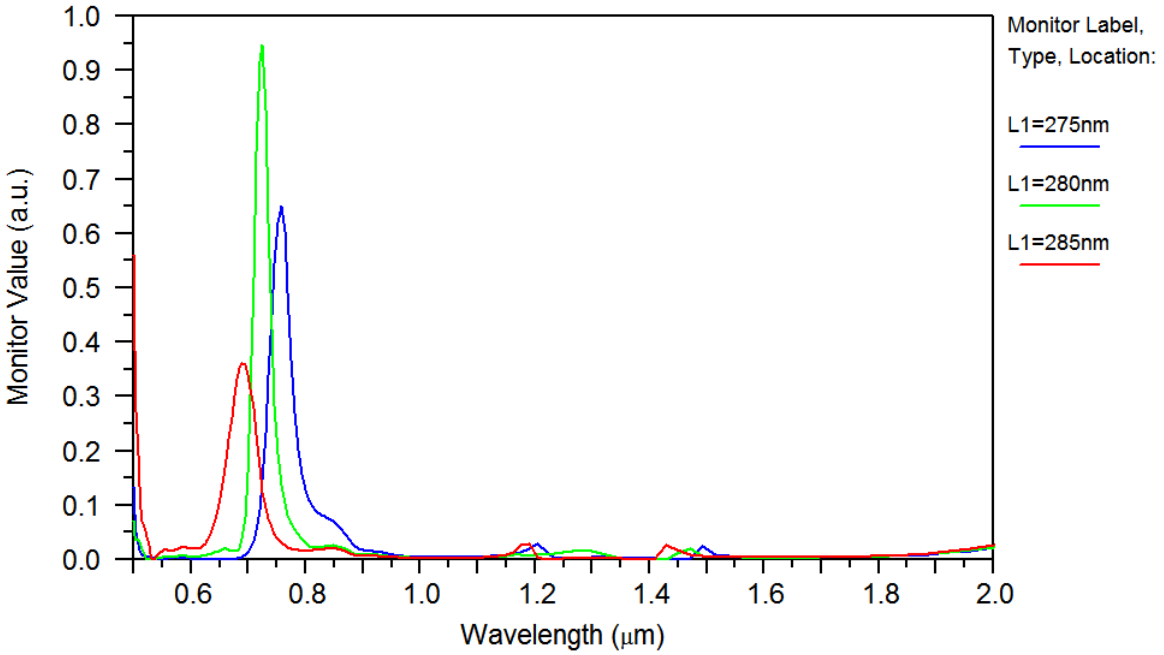

Figure III.45 transmission spectra of the MIM structure for different values of L1.

It is clear from Figure III.45 that the optimal L1 length is 280nm.

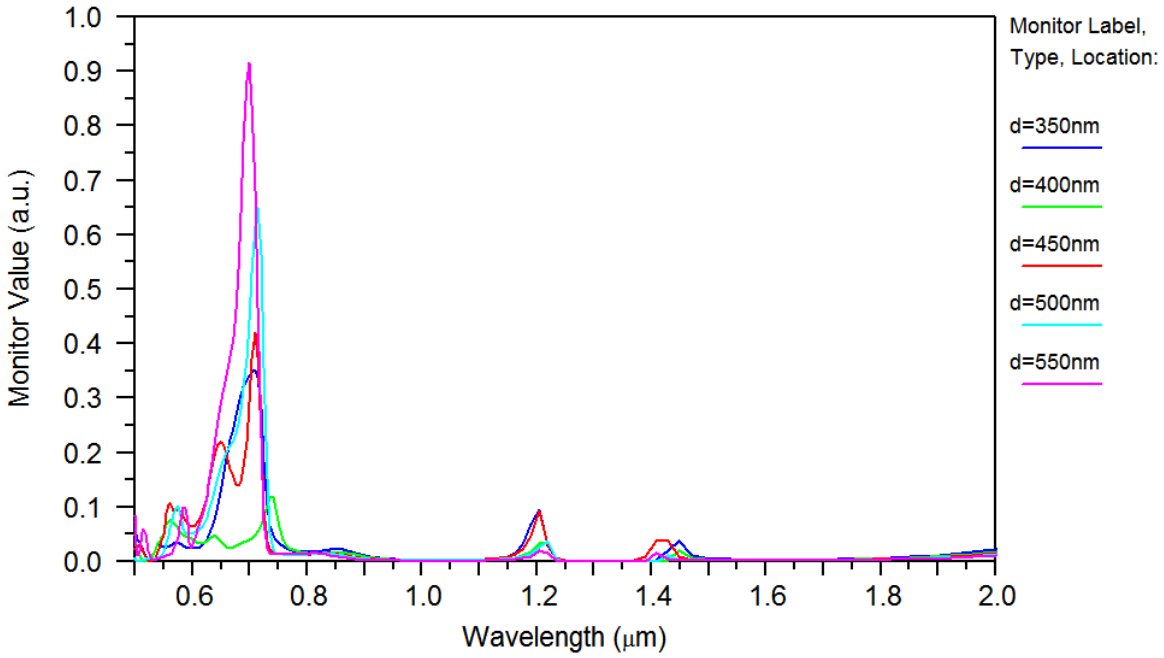

Figure III.46 transmission spectra of the MIM structure for different values of d.

Here in Figure III.46 we observe that the best "d" length for a good transmission is d=550nm

III.5.1.b Structure Sensitivity:

The sensor sensitivity and the quality factor Q, are respectively defined as $S = \Delta\lambda/\Delta n$ and $Q = \lambda/FWHM$. The transmission spectra of the MIM studied structure is shown in the figure III.15, and the calculated sensitivity S is given in the Table III.3 respectively.

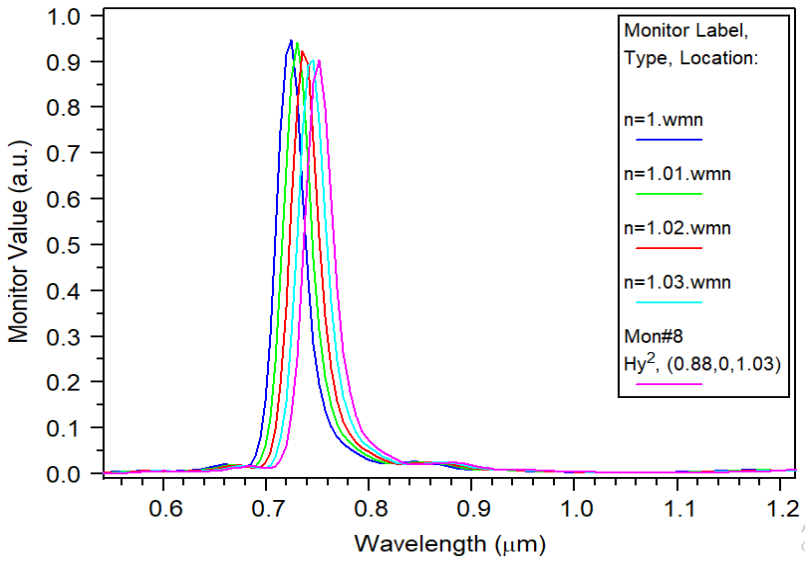

Figure III.47 The structure Transmission response of for different refractive indexes.

-Quality factor **Q** of this structure at λ=722nm:

$$Q = \lambda/FWHM$$

$$\Rightarrow 0.722 \div (0.735 - 0.7113) = 30.464135021$$

The refractive index for structure 01	Wavelength (µm)	Sensitivity
1	**722nm**	**S1=1100nm/RIU** **S2=900nm/RIU** **S3=900nm/RIU** **S4=1200nm/RIU**
1.01	**733nm**	
1.02	**742nm**	
1.03	**751nm**	
1.04	**763nm**	

Table III.3 Sensitivity (nm / RIU) as a function of the change in refractive index.

III.6. Conclusion

This Chapter proposes and investigates a novel plasmonic temperature-sensing structure constructed by a dual MIM waveguide with symmetric coupled cavity and defect. The sensor consists of a main bus-waveguide for connection of input and output, and a rectangular is designed in its proximity.

The simulation results by using the FDTD method show that the FWHM of the resonance dip can be narrowed down by decreasing the coupling distance between the MIM waveguide and the cavities, and a maximum extinction ratio can be obtained at an appropriate position. The temperature-sensing characteristics are testing based on the relationship between the refractive index of the dielectric material and the environment temperature.

The simulation of this sensor shows that its sensitivity can reach an order of magnitude of 1100nm / URI, assuming a wavelength resolution of 0.01 nm. The sensor could be applied for high resolution temperature detection due to its high resolution. In detection applications, calculations show that the sensitivity of the proposed structure is approximately 1100 and 1200 nm / RIU.

This compact plasmonic structure with very high merit level could find important applications in nano sensors on chip. The structure involves a configuration which is suitable for the application where the simultaneous detection of analyte is required. The results showed that any increase in the length and size of the ring leads to a red-shift in the filtered wavelength.

General conclusion

The main objective of this work is the conception and the study of a plasmonic based sensor for the specific application as temperature sensor with the help of RSoft software.

Along the thesis firstly we provided in the beginning of the thesis an explanation of plasmonics phenomenon starting with its definition and its properties with the describing equations also the excitation and coupling of surface plasmons and their waveguiding to have a basic understanding of this technology and then secondly we described the implementation of this phenomenon in sensors and the characteristics of these sensors such as sensitivity and figure of merit along modeling methods and a example of a MIM temperature sensor lastly a presentation of the CAD software RSoft with some explanation of how to use it then our proposed structure modeling, simulation and results which shows that its sensitivity can reach an order of 1100nm / URI, assuming a wavelength resolution of 0.01 nm. The sensor can be implemented for high resolution temperature detection due to its high resolution where conventional sensors can't be used.

In summary a novel sensor structure based on a metal–insulator–metal (MIM) waveguide (using the plasmon surface resonance "SPR") coupled with a cavity then a defect is studied and presented that have high sensitivity and resolution that can be implemented in high resolution temperature sensing.

References:

1. R.W. Wood (1902) XLII. *On a remarkable case of uneven distribution of light in a diffraction grating spectrum*, The London, Edinburgh, and Dublin Philosophical Magazine and Journal of Science, 4:21, 396-402, DOI: 10.1080/14786440209462857

2. U. Fano, "The Theory of Anomalous Diffraction Gratings and of Quasi-Stationary Waves on Metallic Surfaces (Sommerfeld's Waves)," J. Opt. Soc. Am. 31, 213-222 (1941).

3. D. Pines, "Collective Energy Losses in Solids," Rev. Mod. Phys. 28, 184–198 (1956).

4. T. Turbadar, 1959," Oblique reflectance and transmittance measurements on aluminum films", Vacuum,Volume 9, Issue 2, 139-143,

5. Otto, A.,(1968). "Excitation of Nonradiative Surface Plasma Waves in Silver by Method of Frustrated Total Reflection". European Physical Journal A. 216. 398-410. 10.1007/BF01391532.

6. Kretschmann, E. and Raether, H. (1968) "Radiative Decay of Nonradiative Surface Plasmons Excited by Light." Zeitschrift für Naturforschung A, 23, 2135-2136. http://dx.doi.org/10.1515/zna-1968-1247

7. I. Pockrand, J.D. Swalen, J.G. Gordon, M.R. Philpott,1978,"Surface plasmon spectroscopy of organic monolayer assemblies",Surface Science, 74:1, 237-244, https://doi.org/10.1016/0039-6028(78)90283-2

8. DIETER M. KOLB, 1982, "CHAPTER 8 - The Study of Solid-Liquid Interfaces by Surface Plasmon Polariton Excitation", Editor(s): V.M. AGRANOVICH, D.L. MILLS, Modern Problems in Condensed Matter Sciences, Elsevier, 1, 299-329, https://doi.org/10.1016/B978-0-444-86165-8.50014-1.

9. P. Berini, "Plasmon-polariton waves guided by thin lossy metal films of finite width: Bound modes of symmetric structures," Phys. Rev. B 61, 10484–10503 (2000).

10. Linden S, Enkrich C, Wegener M, Zhou J, Koschny T, Soukoulis CM. Magnetic response of metamaterials at 100 terahertz. *Science*. 2004;306(5700):1351-1353. doi:10.1126/science.1105371.
11. Maier, S. A., Springer: New York, 2007. Plasmonics: Fundamentals and Applications.

12. Vial, A.; Grimault, A. S.; Macias, D.; Barchiesi, D.; de la Chapelle, M. L. Physical Review B. 2005,71. Improved analytical fit of gold dispersion: Application to the modeling of extinction spectra with a finite-difference time-domain method.

13. Ritchie, R. H. Physical Review. 1957,106, 874-881. Plasma losses by fast electrons in thin films.

14. J. Homola, Surface Plasmon Resonance Based Sensors (Springer, 2006).

15. Homola, J. Chemical Reviews. 2008,108, 462-493. Surface plasmon resonance sensors for detection of chemical and biological species.

16. Zayats, A. V.; Smolyaninov, II; Maradudin, A. A. Physics Reports-Review Section of Physics Letters. 2005,408, 131-314. Nano-optics of surface plasmon Polaritons.

17. Ritchie, R. H.; Arakawa, E. T.; Cowan, J. J.; Hamm, R. N. Physical Review Letters. 1968,21, 1530-1533. Surface-plasmon resonance effect in grating diffraction.

18. Renger, J.; Quidant, R.; van Hulst, N.; Palomba, S.; Novotny, L. Physical Review Letters. 2009,103. Free-Space Excitation of Propagating Surface Plasmon Polaritons by Nonlinear Four-Wave Mixing.

19. Snyder AW, Love JD (1983) Optical waveguide theorie, Chap viii. Science paper-backs 190. Chapman and Hall, London New York, p 734.

20. Englebienne, P. Analyst. 1998,123, 1599-1603. Use of colloidal gold surface plasmon resonance peak shift to infer affinity constants from the interactions between protein antigens and antibodies specific for single or multiple epitopes.

21. E. N. Economou, “Surface plasmons in thinfilms,” Phys. Rev., vol. 182, no. 2, pp. 539-554, Jun. 1969.

22. B. Prade, J. Y. Vinet, and A. Mysyrowicz, “Guided optical waves in planar heterostructures with negative dielectric-constant,” Phys. Rev. B, vol. 44, no. 24, pp. 13 556-13 572, Dec. 1991.

23. P. B. Johnson and R. W. Christy, “Optical-constants of noble-metals,” Phys. Rev. B, vol.6, no. 12, pp. 4370-4379, Dec. 1972.

24. J. A. Dionne, H. J. Lezec, and H. A. Atwater, “Highly confined photon transport in subwavelength metallic slot waveguides,” Nano Lett., vol. 6, no. 9, pp. 1928-1932, Sep. 2006.

25. T. Goto, Y. Katagiri, H. Fukuda, H. Shinojima, Y. Nakano, I. Kobayashi, and Y. Mitsuoka, “Propagation loss measurement for surface plasmon-polariton modes at metal waveguides on semiconductor substrates,” Appl. Phys. Lett., vol. 84, no. 6, pp. 852-854, Feb. 2004.

26. P. Berini, "Long-range surface plasmon polaritons," Adv. Opt. Photon. 1, 484–588 (2009).

27. J. C. Weeber, Y. Lacroute, and A. Dereux, “Optical nearfield distributions of surface plasmon waveguide modes,” Phys. Rev. B, vol. 68, no. 11, p. 115401, Sep. 2003.

28. S. I. Bozhevolnyi, V. S. Volkov, E. Devaux, and T. W. Ebbesen, “Channel plasmon-polariton guiding by subwavelength metal grooves,” Phys. Rev. Lett., vol. 95, no. 4, p. 046802, Jul.2005.

29. S. A. Maier, Plasmonics: Fundamentals and Applications. Berlin: Springer, 2007.

30. J. Homola, “Present and future of surface plasmon resonance biosensors,” Anal. Bioanal. Chem., vol. 377, pp. 528–539, 2003.

31. I. Abdulhalim, M. Zourob, and A. Lakhtakia, “Surface plasmon resonance for biosensing: a mini-review,” Electromagnetics, vol. 28, pp. 214–242, 2008.

32. J.N.Anker, W.P.Hall, O.Lyandersetal.,“Biosensing with plasmonic nanosensors, ”Nature Mater., vol. 7, pp. 442–453, 2008.

33. M. E. Stewart, C. R. Anderton, L. B. Thompson et al., “Nanostructured plasmonic sensors,” Chem. Rev., vol. 108, pp. 494–521, 2008

34. B. Sep´ulveda, P. C. Angelom´e, L. M. Lechuga, and L. M. Liz-Marz´an, “LSPR-based nanobiosensors,” Nano Today, vol. 4, pp. 244–251, 2009.

35. T. W. Ebbesen, H. J. Lezec, H. F. Ghaemi, T. Thio, and P. A. Wolff, “Extraordinary optical transmission through sub-wavelength hole arrays,” Nature, vol. 391, pp. 667–669, 1998.

36. H. F. Ghaemi, T. Thio, D. E. Grupp, T. W. Ebbesen, and H. J. Lezec, “Surface plasmons enhanceopticaltransmissionthroughsubwavelengthholes,”Phys.Rev.B,vol.58,pp.6779–6782, 1998.

37. A. Degiron, H. J. Lezec, W. L. Barnes, and T. W. Ebbesen, “Effects of hole depth on enhanced light transmission through subwavelength hole arrays,” Appl. Phys. Lett., vol. 81, pp. 4327–4329, 2002.
38. W. L. Barnes, W. A. Murray, J. Dintinger, E. Devaux, and T. W. Ebbesen, “Surface plasmon polaritons and their role in the enhanced transmission of light through periodic arrays of subwavelength holes in a metal film,” Phys. Rev. Lett., vol. 92, 107401, 2004.
39. [11] J. Prikulis, P. Hanarp, L. Olofsson, D. Sutherland, and M. Kall, “Optical spectroscopy of nanometric holes in thin gold films,” Nano Lett., vol. 4, pp. 1003–1007, 2004.
40. H. J. Lezec and T. Thio, “Diffracted evanescent wave model for enhanced and suppressed optical transmission through subwavelength hole arrays,” Opt. Express, vol. 12, pp. 3629– 3651, 2004.
41. A.Degironand T.W.Ebbesen, “The role of localized surface plasmon modes in the enhanced transmission of periodic subwavelength apertures, ”J.Opt .A: PureAppl. Opt., vol.7, pp.S90– S96, 2005.
42. C. Genet and T. W. Ebbesen, “Light in tiny holes,” Nature, vol. 445, pp. 39–46, 2007.
43. F.J.Garcia-Vidal, L.Martin-Moreno, T.W.Ebbesen,and L.Kuipers, “Light passing through subwavelength apertures,” Rev. Mod. Phys., vol. 82, pp. 729–787, 2010.
44. T. Sannomiya, O. Scholder, K. Jefimovs, C. Hafner, and A. B. Dahlin, “Investigation of plasmon resonances in metal films with nanohole arrays for biosensing applications,” Small, vol. 7, pp. 1653–1663, 2011.
45. K.-L. Lee, C.-W. Lee, W.-S. Wang, and P.-K. Wei, “Sensitive biosensor array using surface plasmon resonance on metallic nanoslits,” J. Biomed. Opt., vol. 12, 044023, 2007.
46. N. Liu, T. Weiss M. Mesch et al., “Planar metamaterial analogue of electromagnetically induced transparency for plasmonic sensing,” Nano Lett., vol. 10, pp. 1103–1107, 2010.
47. P. Offermans, M. C. Schaafsma, S. R. K. Rodriguez et al., “Universal scaling of the figure of merit of plasmonic sensors,” ACS Nano, vol. 5, pp. 5151–5157, 2011.
48. Z. Fang, J. Cai, Z. Yan et al., “Removing a wedge from a metallic nanodisk reveals a Fano resonance,” Nano Lett., vol. 11, pp. 4475–4479, 2011.

49. W.-S. Chang, J. B. Lassiter, P. Swanglap et al., “A plasmonic Fano switch,” Nano Lett., vol. 12, pp. 4977–4982, 2012.
50. Y. Wang, A. Brunsen, U. Jonas, J. Dostlek, and W. Knoll, “Prostate specific antigen biosensor based on long range surface plasmon-enhanced fluorescence spectroscopy and dextran hydrogel binding matrix,” Anal. Chem., vol. 81, pp. 9625–9632, 2009.
51. X. F. Li and S. F. Yu, “Extremely high sensitive plasmonic refractive index sensors based on metallic grating,” Plasmonics, vol. 5, pp. 389–394, 2010.
52. M. J. Levene, J. Korlach, S. W. Turner et al., “Zero-mode waveguides for single-molecule analysis at high concentrations,” Science, vol. 299, pp. 682–686, 2003.
53. Guillaume Baffou, Romain Quidant et Christian Girard. « Thermoplasmonics modeling : A Green’s function approach ». en. In : Physical Review B 82.16 (oct. 2010). doi : 10.1103/PhysRevB.82.165424. url :http://link. aps.org/doi/10.1103/PhysRevB.82.165424 (visité le 07/12/2014) (cf. p. 30, 43, 81, 172, 175).
54. Pierre Bon, Nadia Belaid, Denis Lagrange, Christian Bergaud, Hervé Rigneault, Serge Monneret et Guillaume Baffou. « Three-dimensional temperature imaging around a gold microwire ». In : Applied Physics Letters 102.24 (2013), p. 244103. url : http://scitation.aip.org/content/aip/ journal/apl/102/24/10.1063/1.4811557 (visité le 23/05/2014) (cf. p. 30).
55. Michael T. Carlson, Aurangzeb Khan et Hugh H. Richardson. « Local Temperature Determination of Optically Excited Nanoparticles and Nanodots ». en. In : Nano Letters 11.3 (mar. 2011), p. 1061–1069. doi : 10.1021/ nl103938u. url : http : / / pubs . acs . org / doi / abs / 10 . 1021 / nl103938u (visité le 24/11/2016) (cf. p. 38, 147).
56. O.A. Yeshchenko, I.S. Bondarchuk, V.S. Gurin, I.M. Dmitruk et A.V. Kotko. « Temperature dependence of the surface plasmon resonance in gold nanoparticles ». en. In : Surface Science 608 (fév. 2013), p. 275–281. doi : 10.1016/j.susc.2012.10.019. url : http://linkinghub.elsevier.com/ retrieve/pii/S0039602812003895 (visité le 23/05/2014) (cf. p. 38, 39).
57. F. Eftekhari, C. Escobedo, J. Ferreira et al., “Nanoholes as nanochannels: Flow-through plasmonic sensing,” Anal. Chem., vol. 81, pp. 4308–4311, 2009.

58. A. A. Yanik, M. Huang, A. Artar, T. Y. Chang, and H. Altug, "Integrated nanoplasmonic– nanofluidic biosensors with targeted delivery of analytes," Appl. Phys. Lett., vol.96,021101, 2010.
59. M. Yamamoto, "Surface plasmon resonance (SPR) theory: tutorial," Rev. Polarography, vol. 48, pp. 209–237, 2002.
60. L. Wu, P. Bai, and E. P, Li, "Designing surface plasmon resonance of subwavelength hole arrays by studying absorption," J. Opt. Soc. Am. B, vol. 29, pp. 521–528, 2012.
61. E. D. Palik, Ed., Handbook of Optical Constants of Solids. San Diego, CA: Academic Press, 1991.
62. L. Wu, H. S. Chu, W. S. Koh, and E. P, Li, "Highly sensitive graphene biosensors based on surface plasmon resonance," Opt. Express, vol. 18, pp. 14395–14400, 2010.
63. B. Song, D. Li, W. P. Qi et al., "Graphene on Au(111): A highly conductive material with excellent adsorption properties for high-resolution bio/nanodetection and identification," ChemPhysChem, vol. 11, pp. 585–589, 2010.
64. G. B. McGaughey, M. Gagn´e, and A. K. Rapp´ e, π "pi-Stacking interactions alive and well in proteins," J. Biol. Chem., vol. 273, pp. 15458–15463, 1998.
65. Z. Tang, H. Wu, J. R. Cort et al., "Constraint of DNA on functionalized graphene improves its biostability and specificity," Small, vol. 6, pp. 1205–1209, 2010.
66. M. Bruna and S. Borinia, "Optical constants of graphene layers in the visible range," Appl. Phys. Lett., vol. 94, 031901, 2009.
67. L. Wu, P. Bai, X. Zhou, and E. P, Li, "Reflection and transmission modes in nanohole-array based plasmonic sensors," IEEE Photon. J., vol. 3, pp. 441–449, 2012.
68. A. A. Yanik, M. Huang, O. Kamohara et al., "An optofluidic nanoplasmonic biosensor for direct detection of live viruses from biological media," Nano Lett., vol. 10, pp. 4962–4969, 2010.
69. B. Hapke, Theory of Reflectance and Emittance Spectroscopy. Cambridge: Cambridge University Press, 1993.
70. J.-P. Berenger, A perfectly matched layer for the absorption of electromagnetic waves, Journal of computational physics 114 (2).185200. 2.5.2 (1994).

71. B. Abderrahmane, Extension de la modelisation par fdtd en nano-optique, Ph.D. thesis, Universit´e de Franche-comte. UFR des sciences et techniques . 2.5.2(2008).
72. D. Hall, “Use of optical biosensors for the study of mechanically concerted surface adsorption processes,” Analytical Biochemistry 288, pp. 109-125 (2001).
73. Melle Benaissa Fatima, Etude et Simulation de la Propagation des Ondes Electromagnetiques dans les guides a Cristaux Photoniques-Application aux Fibres Optiques Memoire de Magister, Universite ABOU-BAKR BELKAID, Tlemcen, 2013.
74. Xie, Y.Y. ; Huang, Y.X. ; Zhao, W.L. ; Xu, W.H. ; He, C. IEEE Photon. J, 7, 4800612-1–4800612-12. 2015 1695.
75. Maier, S.A. Plasmonics : Fundamentals and Applications ; Springer : New York, (2007).